CloudRoots-Amazon22: Integrating Clouds with Photosynthesis by Crossing Scales

J. Vilà-Guerau de Arellano [ORCID],[a,m] O. K. Hartogensis,[a] H. de Boer,[b] R. Moonen,[c]
R. González-Armas,[a] M. Janssens,[a] G. A. Adnew,[c] D. J. Bonell-Fontás,[c] S. Botía,[d]
S. P. Jones,[e] H. van Asperen,[e] S. Komiya,[e] V. S. de Feiter,[a] D. Rikkers,[a] S. de Haas,[a]
L. A. T. Machado,[f,g] C. Q. Dias-Junior,[h] G. Giovanelli-Haytzmann,[g] W. I. D. Valenti,[i]
R. C. Figueiredo,[i] C. S. Farias,[i] D. H. Hall,[i] A. C. S. Mendonça,[i] F. A. G. da Silva,[f]
J. L. Marton da Silva,[j] R. Souza,[k] G. Martins,[i] J. N. Miller,[l] W. B. Mol,[a] B. Heusinkveld,[a]
C. C. van Heerwaarden,[a] F. A. F. D'Oliveira,[h] R. Rodrigues Ferreira,[n] R. Acosta Gotuzzo,[o]
G. Pugliese,[m] J. Williams,[m,p] A. Ringsdorf,[m] A. Edtbauer,[m] C. A. Quesada,[i]
B. Takeshi Tanaka Portela,[i] E. Gomes Alves,[e] C. Pöhlker,[g] S. Trumbore,[e]
J. Lelieveld,[m] and T. Röckmann[c]

ABSTRACT: How are rain forest photosynthesis and turbulent fluxes influenced by clouds? To what extent are clouds affected by local processes driven by rain forest energy, water, and carbon fluxes? These interrelated questions were the main drivers of the intensive field experiment CloudRoots-Amazon22 which took place at the Amazon Tall Tower Observatory (ATTO)/Campina supersites in the Amazon rain forest during the dry season, in August 2022. CloudRoots-Amazon22 collected observational data to derive cause–effect relationships between processes occurring at the leaf level up to canopy scales in relation to the diurnal evolution of the clear-to-cloudy transition. First, we studied the impact of cloud and canopy radiation perturbations on the sub-diurnal variability of stomatal conductance. Stoma opening is larger in the morning, modulated by the cloud optical thickness. Second, we combined 1-Hz frequency measurements of the stable isotopologues of carbon dioxide and water vapor with measurements of turbulence to determine carbon dioxide and water vapor sources and sinks within the canopy. Using scintillometer observations, we inferred 1-min sensible heat flux that responded within minutes to the cloud passages. Third, collocated profiles of state variables and greenhouse gases enabled us to determine the role of clouds in vertical transport. We then inferred, using canopy and upper-atmospheric observations and a parameterization, the cloud cover and cloud mass flux to establish causality between canopy and cloud processes. This shows the need for a comprehensive observational set to improve weather and climate model representations. Our findings contribute to advance our knowledge of the coupling between cloudy boundary layers and primary carbon productivity of the Amazon rain forest.

AFFILIATIONS: [a] Meteorology and Air Quality Section, Wageningen University, Wageningen, Netherlands; [b] Environmental Sciences, Copernicus Institute of Sustainable Development, Utrecht University, Utrecht, Netherlands; [c] Institute Marine and Atmospheric Utrecht, Utrecht University, Utrecht, Netherlands; [d] Biogeochemical Signals Department, Max Planck Institute for Biogeochemistry, Jena, Germany; [e] Biogeochemical Processes Department, Max Planck Institute for Biogeochemistry, Jena, Germany; [f] Institute of Physics, University of São Paulo, São Paulo, Brazil; [g] Multiphase Chemistry Department, Max Planck Institute for Chemistry, Mainz, Germany; [h] Physics Department (IFPA), Federal Institute of Pará, Belém, Pará, Brazil; [i] Instituto Nacional de Pesquisas da Amazônia, Manaus, Brazil; [j] Instituto Nacional de Pesquisas Espaciais, Cachoeira Paulista, Brazil; [k] Univerisidae do Estado do Amazonas, Manaus, Brazil; [l] NOAA/ESRL Global Monitoring, Boulder, Colorado; [m] Atmospheric Chemistry Department, Max Planck Institute for Chemistry, Mainz, Germany; [n] Amazon Tall Tower Observatory, Program Large Scale Biosphere-Atmosphere in the Amazon (LBA), Manaus, Amazonas, Brazil; [o] Federal University of Rio Grande, Rio Grande, Brazil; [p] Climate and Atmosphere Research Center, The Cyprus Institute, Nicosia, Cyprus

1. Introduction

In the Amazon basin, clouds and the canopy mediate the exchange of energy, water, and carbon dioxide between the rain forest and the atmosphere. The processes underlying these fluxes are connected in complex ways that are not well understood. Yet, they are key to understand the basin's response to stress and its resilience under current effects of deforestation, regional warming, and enhancement of carbon dioxide (CO_2) levels (Costa and Foley 2000). Regulated by vegetation processes, rainfall patterns over large portions of the basin are currently disrupted due to an increased water vapor deficit (Barkhordarian et al. 2019), lengthening of the dry season (Fu et al. 2013), and the replacement of forest with pasture or crops (Spracklen et al. 2012). More specific to the carbon cycle, biomass observations indicate a declining trend of CO_2 assimilation by the Amazon forest due to its low resilience to climate extremes such as drought (Brienen et al. 2015; Hubau et al. 2020). Due to the coupling between energy, water, and carbon canopy fluxes, a decrease in CO_2 uptake leads to a decline in evaporation and an increase of the sensible heat flux (Biudes et al. 2015; Longo et al. 2020). These shifts in canopy fluxes alter the transport of moisture into the cloud layer influencing key processes associated to rain formation (Sikma and Vilà-Guerau de Arellano 2019). In turn, these shifts are strongly modulated by synoptic and mesoscale weather patterns (Machado 2000). Looking into our near future climate, these local-to-regional atmospheric scales of motions are influenced by the current enhancement of atmospheric warming and of CO_2 concentrations (Sikma et al. 2019).

Every molecule of water and CO_2 that is exchanged passes through tiny openings in the soil and the stomata of leaves (Roberts et al. 1990). This process regulates the partition of available radiative energy in sensible and latent heat fluxes above the canopy, that in turn governs the intensity and nature of turbulence (Moene and van Dam 2014). Turbulent thermals organize the transport of heat, moisture, and carbon inside the canopy (Patton et al. 2016) and through the atmospheric boundary layer (ABL). This leads to the formation and intensification of cumulus clouds (Martin et al. 1988; Ouwersloot et al. 2013). In all, cumulus clouds formed by this chain of processes are rooted in the biosphere, giving our project its name—CloudRoots—which echoes and extends the early interaction studies between cumulus clouds and the subcloud layer in the marine trade-wind region (LeMone and Pennel 1976). By extending the "roots," we aim not only to study how the canopy influences clouds but also how clouds modify the canopy fluxes.

Photosynthesis regulates the canopy turbulent exchange, and it is governed by the diurnally varying solar radiation through a broken cloud field (Pedruzo-Bagazgoitia et al. 2017; Kivalov and Fitzjarrald 2018; Durand et al. 2021) and the turbulence in and above the canopy (Patton et al. 2016). Even though these individual biophysical processes governing the exchange between the vegetation and cloudy boundary layer are identified and previously investigated, current understanding and representation of the interaction between rain forest fluxes and cloudy atmospheres are limited due to the barriers between disciplines (Vilà-Guerau de Arellano et al. 2023). To overcome these, we need to interconnect biophysical processes across spatiotemporal scales, from regional weather patterns to local and vertical transport and exchanges processes, as shown in Figs. 1a,b, respectively. To advance our understanding, here, we focus on processes occurring at the scales of leaves to canopies to clouds, and temporal variability from the time it takes for a cloud shadow to pass (seconds to minutes), to the diurnal cycle (Fig. 1b). These spatiotemporal scales are coarsely represented and resolved in contemporary weather and climate models, casting doubt on the fluxes (magnitude and diurnal variability) they predict, as discussed by Bonan et al. (2021) and Friedlingstein et al. (2022).

The CloudRoots-Amazon22 field experiment was conceived to quantify which processes, ranging from stomatal conductance to clouds, are essential to understand and represent the partition of available radiation into the canopy fluxes of energy, water, and carbon and their coupling to clouds. To this end, our research strategy is to take collocated and comprehensive measurements designed to quantify the bidirectional responses between canopy fluxes and clouds across the diurnal cycle. Specifically, we seek answers to the following questions:

1) To what extent are rain forest photosynthesis and turbulent fluxes of energy, water, and CO_2 influenced by the presence of shallow cumulus clouds?
2) To what extent are clouds affected by small-scale variability (seconds to hours) in rain forest energy, water, and carbon fluxes?

Previous field campaigns paved the way to CloudRoots-Amazon22. Most notably, we highlight the Amazon Boundary Layer Experiment (ABLE-2A). This field study paved the way for our field campaign by relating local-to-regional motion scales, integrating the physics (Fitzjarrald et al. 1988) and chemistry (Harriss et al. 1990) of the rain forest and
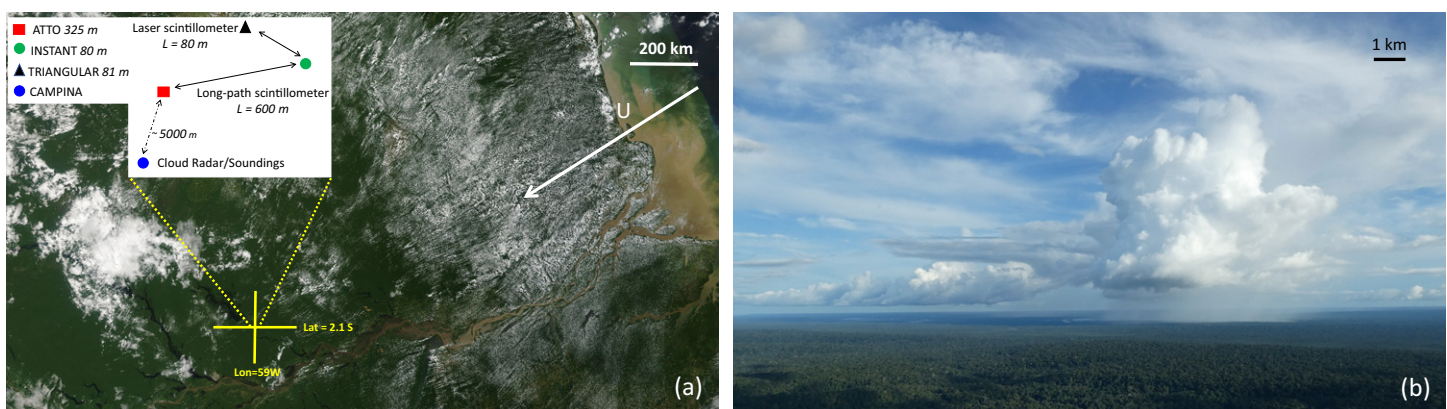

FIG. 1. (left) Moderate Resolution Imaging Spectroradiometer (MODIS) scene from 16 Aug 2022 characterized by ShDeep convection at the ATTO–Campina supersites. The average wind speed ranges from 4 to 6 m s^{-1}, and wind direction was predominately northeast. The CloudRoots-Amazon22 area including the ATTO and Campina site are indicated by the yellow cross. The insight figure shows the distance between the ATTO and Campina supersites and the location of the laser- and long-path scintillometer. (right) Impression of a precipitating cloud that shades the surface above the supersites of ATTO and Campina. Map scale is shown at the top right of both figures.

connected to the atmospheric boundary layer. Other influential and related field studies are the comprehensive CHUVA program on cloud processes and their relation to tropical weather forecasting (Machado et al. 2014), the link between urban Manaus and pristine conditions on atmospheric chemistry during the GoAmazon2014/5 campaign (Martin et al. 2017), and, recently, the Chemistry of the Atmosphere: Field Experiment in Brazil (CAFE-Brazil) campaign (December 2022–February 2023) on new cloud particle formation and the impact of deep convection. Our research design was also strongly inspired by the pioneering compendium written by Garstang and Fitzjarrald (1999), the comprehensive research on the Amazon as a physical, biological system within the program Large-Scale Biosphere–Atmosphere Experiment in the Amazon (LBA) (Avissar et al. 2002), and a review on the topic by Gentine et al. (2019).

Here, we provide an overview of the observations from the CloudRoots-Amazon22 campaign, placing special emphasis on its unique aspect of CloudRoots-Amazon22 with respect to the previous field campaigns: to integrate observations and simulating efforts (Patton et al. 2016; Pedruzo-Bagazgoitia et al. 2023) to study simultaneously ecophysiological processes and canopy fluxes as part of the energy, carbon, and water cycles that interact with clouds. First, we show new observations on the subdiurnal asymmetry of the stomatal conductance (10–100 μm) connected to disruptions of the radiative and turbulent fluxes in relation to vegetation responses and clouds (seconds). Second, we analyze the turbulent (seconds) and subdiurnal vertical evolution (minutes) of stable isotopologues of carbon dioxide and water vapor in and above the canopy and discuss our preliminary results in relation to the emerging challenge to quantify the individual contributions of soil and vegetation to evaporation and the net ecosystem exchange disrupted by the presence of clouds. Third, we relate observations on the diurnal development of shallow and deep convection to the thermodynamic structure and the carbon dioxide profiles up to the midtroposphere ($\sim$5 km). Finally, the causal relationships between canopy fluxes and cloud properties are investigated by a conceptual atmospheric model coupled to the diurnal rain forest conditions. By so doing, we plan to identify relevant and potentially missing processes and aim to evaluate and design new representations of biophysical processes in weather and climate models.

2. Connecting and collocating leaf-to-cloud observations as a continuum

a. Continuous observations at ATTO and Campina supersites. CloudRoots-Amazon22 was conducted from 8 to 21 August 2022, at and around the measurements sites of Amazon Tall Tower Observatory (ATTO) (latitude −2.1458, longitude −59.0055) and Campina (latitude −2.1819, longitude −59.0217). These locations are situated approximately 150 km north of the city of Manaus and approximately 1000 km inland from the Atlantic Ocean. As described by Andreae et al. (2015), both sites are located at Uatumã Sustainable Development Reserve (USDR) in the central Amazon. This region is characterized by different ecosystems: terra firme forests on ancient river terraces, campinas (savanna on white-sand soils), and campinaranas (white-sand forest). Focusing on the terra firme rain forest, the canopy height ranges between 35 and 45 above ground level. In our study, we take 40 m as the average reference canopy height. Figure 1a shows the location of the towers and the area in which the radiosondes and boundary layer flights (vertical profiles and horizontal rasters) took place. Our observational strategy aimed to extend and complete the comprehensive measurements taken routinely at the ATTO and Campina supersites. In short, there are three tall towers at the ATTO facility: ATTO tower (323 m), TRIANGLE tower (triangular mast, 81 m), and INSTANT tower (a guy-wired walk-up tower, 80 m) (Andreae et al. 2015), that continuously measure key profiles of atmospheric state variables (wind, temperature, and specific humidity) and their turbulent fluxes. Shortwave and longwave

radiation is measured at 75 m, and light interception profiles of photosynthetic active radiation (PAR) are gathered across and above the canopy (INSTANT tower). Turbulent fluxes are measured using on-site eddy covariance (EC) techniques that calculate the fluxes at the 30-min time scale.

Regarding greenhouse gases and chemical species, atmospheric composition is routinely measured to constrain the carbon exchange based on measurements of CO_2 (including fluxes), CH_4, and the stable isotopologues of water vapor and CO_2 (see appendix A). The observational dataset of atmospheric chemistry (Nölscher et al. 2016) is completed by measurements of chemically reactive species at 3 heights (80, 150, and 320 m) (Pfannerstill et al. 2021). These species are the most representative biogenic volatile organic compounds (BVOCs): isoprene, the sum of methyl vinyl ketone plus methacrolein and isoprene hydroxyhydroperoxide. The diurnal evolution of measured BVOCs at 3 heights is presented in appendix B. Finally, remote sensing observations at the Campina supersite (Machado et al. 2021), 5 km southeast (SE) from the ATTO tower (Fig. 1a), enabled us to fully characterize the cloud properties such as cloud base, cloud top, liquid water content, vertical velocities, and precipitation over the entire campaign.

b. Leaf and canopy observations specific to CloudRoots-Amazon22. The CloudRoots-Amazon22 campaign added dedicated measurements that provide a full description of the subhourly and diurnal variability of the energy, water, and carbon exchange processes and perturbations affected by the presence of clouds and the canopy rain forest (Table 1). On-site observations of canopy light profiles (400–700 nm) were complemented with vertical profiles gathered by a fast radiation broadband (10 Hz) spectrometer. This spectrometer measures 18 light spectra in 18 wave bands ranging from 400 to 950 nm with a 20-nm full width half maximum bandwidth (Heusinkveld et al. 2023).

To trace the influence of subdiurnal dynamics of inside-canopy gradients in light, temperature, humidity, and CO_2, we measured leaf-level stomatal conductance and photosynthesis

Table 1. Variables measured during the CloudRoots-Amazon22 campaign in addition to the routine standard measurements collected at the super sites ATTO and Campina.

Variables	Spatial scale	Temporal scale	Height	Aim
1) Stomatal conductance	Leaf	Subdiurnal	Discrete measurements Bottom (2 m), middle (between 25 and 30 m), top canopy (between 30 and 40 m)	Diurnal asymmetry
2) Photosynthesis	Leaf	Subdiurnal	Discrete measurements Bottom, middle, and top canopy	Subdiurnal asymmetry Height dependence
3) Soil/leaf water isotopic composition	Soil/leaf	Subdiurnal	Discrete measurements	Plant distribution
4) Soil efflux H_2O and CO_2	Canopy	Hourly–diurnal	Ground surface	Contribution soil efflux to NEE
5) Spectral irradiance 400–950 nm	Canopy	Subsecond–weekly	0.5, 5.77, 15.0, 22.68, 26.84, and 62.91 m	Time cloud and canopy light fluctuations
			0 m (Campina), 2.5 m (Campsite), 63 m (INSTANT), and 322 m (ATTO)	Spatial cloud and canopy light fluctuations
6) Sensible heat flux	Canopy	Minute–hourly	56 m	1-min turbulent fluxes (laser scintillometer)
7) Sensible heat flux	Canopy (hectometer)	Hourly–diurnal	56 m	Hectometer line-averaged fluxes (scintillometer)
8) Isotopologues CO_2 and H_2O	Canopy	Minute–hourly	56 m	1-min turbulent fluxes
9) Profiling state variables (sounding)	Regional	Hourly–diurnal	0 to ~14 000 m	State variable vertical variation
10) Profiling and horizontal raster (aircraft) H_2O, CO_2, CO, and CH_4	Regional	Instantaneous	0 to ~6000 m	Greenhouse gases spatial variation

across three canopy layers for two consecutive days. Leaf-level gas exchange was measured with the LI-6400XT portable photosynthesis system (LI-COR, Lincoln, Nebraska) with chamber settings closely matching ambient temperature, light, and humidity while keeping sample CO_2 constant at 400 ppm. For our measurements, small branches were excised from their respective locations in the canopy and transported quickly (within 1 min) to the leaf chamber. We randomly selected sunlit and shaded leaves at the canopy top (between 20 and 26 m), the upper–mid canopy (between 13 and 19 m), and the understory (from ground to 5 m), respectively. Here, the aim was to quantify how the stomata open and close during the day and at different canopy heights. This enables us to connect stomatal conductance behavior to radiation, including cloud disturbances (enhancement and shading with respect to the clear sky values) and in canopy perturbations, and micrometeorological conditions. These measurements were done in 2 days under different cloud conditions: 11 August is characterized by shallow cumulus, whereas 12 August is characterized by the transition from shallow to deep convection.

To determine turbulent fluxes at a temporal resolution of minutes (van Kesteren et al. 2013), our campaign incorporated a double-beam laser scintillometer (DBLS; short path beam ≈ 100 m that was located at a height of 59 m between INSTANT and TRIANGLE towers; see Fig. 1a). The scintillometer minute-scale fluxes enable us to determine the response of turbulent fluxes to radiation fluctuations imposed by clouds (van Kesteren et al. 2013; Vilà-Guerau de Arellano et al. 2020). In addition, Fig. 1a shows the long-path scintillometer flux measurements (long path ≈ 500 m) and located between INSTANT and ATTO towers at a height of 56.8 m. These line-path measurements allow us to infer the sensible heat flux with a larger footprint than the EC flux observations under the assumption of canopy spatial homogeneity to be able to apply Monin–Obukhov similarity theory (MOST) to infer fluxes from the observed scintillations. The larger footprint of the long-path scintillometer makes it more suitable for intercomparison with fluxes obtained from model simulations. As shown in Table 1 and described in more detail in appendix A, we furthermore measured the H_2O and CO_2 stable isofluxes at a high frequency (10 Hz) (Moonen et al. 2023) with the purpose of determining the contribution of soil evaporation/efflux and plant transpiration/assimilation to the canopy evaporation and NEE.

c. Upper-atmospheric observations specific CloudRoots-Amazon22. To quantify changes in the state variables between the canopy, the subcloud and cloud layers, and the free troposphere, we launched balloon soundings with high temporal frequency (every 3 h) over the course of the campaign. On 18 August, we extended these measurements by additional aircraft measurements of vertical profiles (up to 5000 m) and horizontal spatial distribution of atmospheric composition (H_2O, CO_2, CO, and CH_4) observations during the morning (0900–1100 LT) and afternoon transition (1300–1500 LT), respectively. The horizontal rasters were flown around the ATTO facility at constant height, including flights above the river Uatumã. Both in the morning and afternoon flights, we selected three representative heights in the subcloud layer, cloud layer, and free troposphere and measured at constant height long, horizontal paths (≈20 km).

These upper-atmospheric observations combined with the Campina cloud radar enabled us to group the date by similar situations of shallow cumulus (ShCu) (6) and distinguish them from the shallow-to-deep (ShDeep) convective days (4) (see Table 2). The date 14 August was characterized by the passage of a squall line at around 1100 LT (local time or Amazon time). Here, we were inspired by previous studies in the Amazon basin (Czikowsky and Fitzjarrald 2009) and using similar criteria to classify the days as applied by Henkes et al. (2021). By creating these ensembles, we attempt to propose archetypal cloudy boundary layers coupled to specific rain forest conditions.

August 2022	Convective regime	Event description
9	ShCu	Onset shallow cumuli (10); increased cloud cover (12); first cloud dissipated (14); all clouds dissipated (1630)
10	ShCu	Onset shallow cumuli (0930); increased cloud cover (11); first clouds dissipated (1230); all clouds dissipated (1630)
11	ShCu	Onset shallow cumuli (0830); increased cloud cover (10); first cloud dissipated (1230); deep convection far (1630)
12	ShDeep	Onset shallow cumuli (9); increased cloud cover (10); first cloud dissipated (1230); deep convection (1230–1630)
13	ShDeep	Clouds high altitude (8); dissipation high-level clouds (10); new clouds form (1030); deep convection (1410–1550)
14	ShDeep	High-level clouds present (9); first deep convection (0950); passage squall line (11)
		Shallow and deep convective development (1230–1630); dissipating clouds (1730)
15	ShCu	Onset shallow cumuli (1045); increased cloud formation (12); clouds dissipated (14)
16	ShDeep	Onset shallow cumuli (10); increased cloud cover (12); first clouds dissipated (13); downburst deep convection (14–15)
17	ShCu	Onset shallow cumuli (10); increased cloud cover (1230); first clouds dissipated (15); clouds disappear (17)
18	ShCu	Onset shallow cumuli (10); increased cloud cover (11); first clouds dissipated (15); clouds disappear (1730)

3. Leaf-level processes: Height and subdiurnal variability

The transfer of shortwave and longwave radiation throughout the atmosphere is a crucial process for the land–atmosphere system as it represents the energy input into the ecosystem (Baldocchi and Amthor 2001). Although routine measurements of the upward and downward/short- and longwave radiation components are regularly carried out to determine the radiative budget, and therefore the net available radiation energy (Moene and van Dam 2014), new observational techniques are required to quantify its complex behavior in space and time and unravel any missing features. As an illustration of the complex vertical and temporal variability in the radiative transfer, Fig. 2 shows the evolution of global horizontal
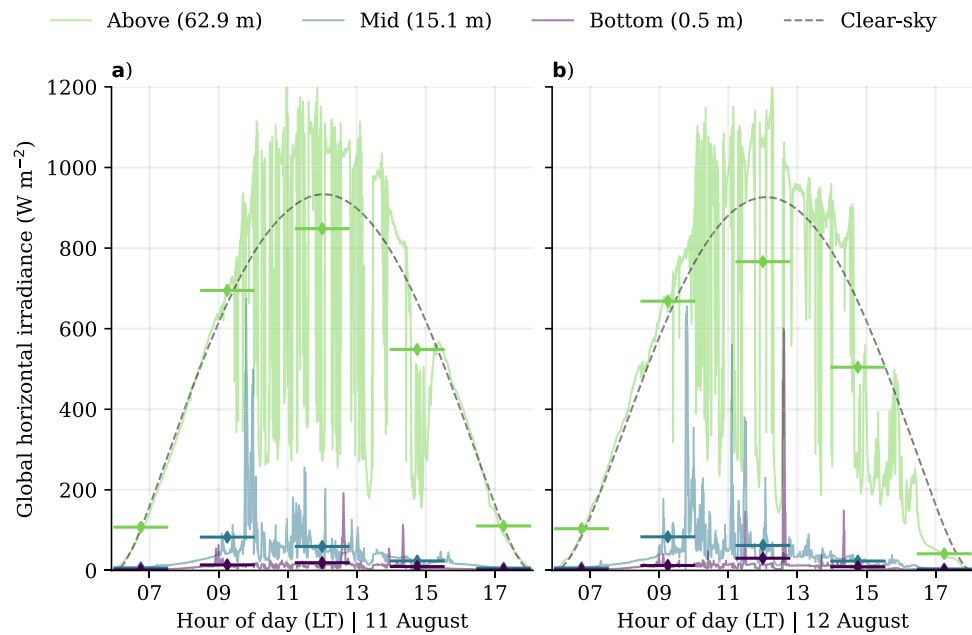

FIG. 2. High-frequency global horizontal irradiance measurements (1 Hz) taken at the 80-m INSTANT tower at three different levels: above canopy (62.9 m), in the middle of canopy (15.1 m), and bottom (0.5 m) during (a) 11 Aug (ShCu) and (b) 12 Aug (ShDeep convection). The average values over the following 1.5-h time intervals are marked by dots: 0600–0730, 0830–1000, 1115–1245, 1400–1530, and 1630–1800 LT. Bars indicate the averaging period (90 min). To be consistent, these periods are the same used for the measurements of the stomatal conductance (shown in Fig. 3). Cloud depth of both days is shown in Fig. C1.

irradiance measured at three representative heights in and above the canopy and compared to the clear-sky calculation for the same day. These observations were selected because they show the simultaneous impact of the passage of shallow (Fig. 2a) and shallow-to-deep clouds (Fig. 2b), characterized by different values of cloud optical thickness (see appendix C), and the disturbances due to the penetration in the canopy. The high-frequency observations enable us to quantify the high variability across a range of scales (from seconds to hours) created by clouds. This is characterized by a significant enhancement of global horizontal irradiance (more than 20%) with respect to not only the clear values by absorption and scattering (Mol et al. 2023) but also the more expected decrease of global irradiance due to cloud shading. The time lag between the radiation perturbation and the reaction of the canopy exchange flux is on the order of minutes (Vilà-Guerau de Arellano et al. 2020). In addition, and as quantified by Kivalov and Fitzjarrald (2019) using observations taken in the Amazon and Harvard temperate forests, these step changes in light can create transient maximum values in the evaporation and net ecosystem exchanges with characteristic time scales of minutes. The strong decrease of the irradiance when penetrating the dense canopy reveals how the complex interplay between disturbances of clouds, plant density distribution, and leaf orientation are key drivers of spatial and temporal variability in ecosystem photosynthesis and transpiration (Parker et al. 2019).

The subdiurnal variability of leaf-level stomatal conductance across the three canopy layers on 11 and 12 August is shown in Fig. 3. Both days show an asymmetric pattern over the course of the day with highest conductance observations before 1300 LT. Similar diurnal behavior was measured in a primary rain forest by Roberts et al. (1990). Under high radiation conditions, and at the canopy top, the decrease on stomatal conductance is due to the high values of temperature and water vapor deficit. The canopy-height
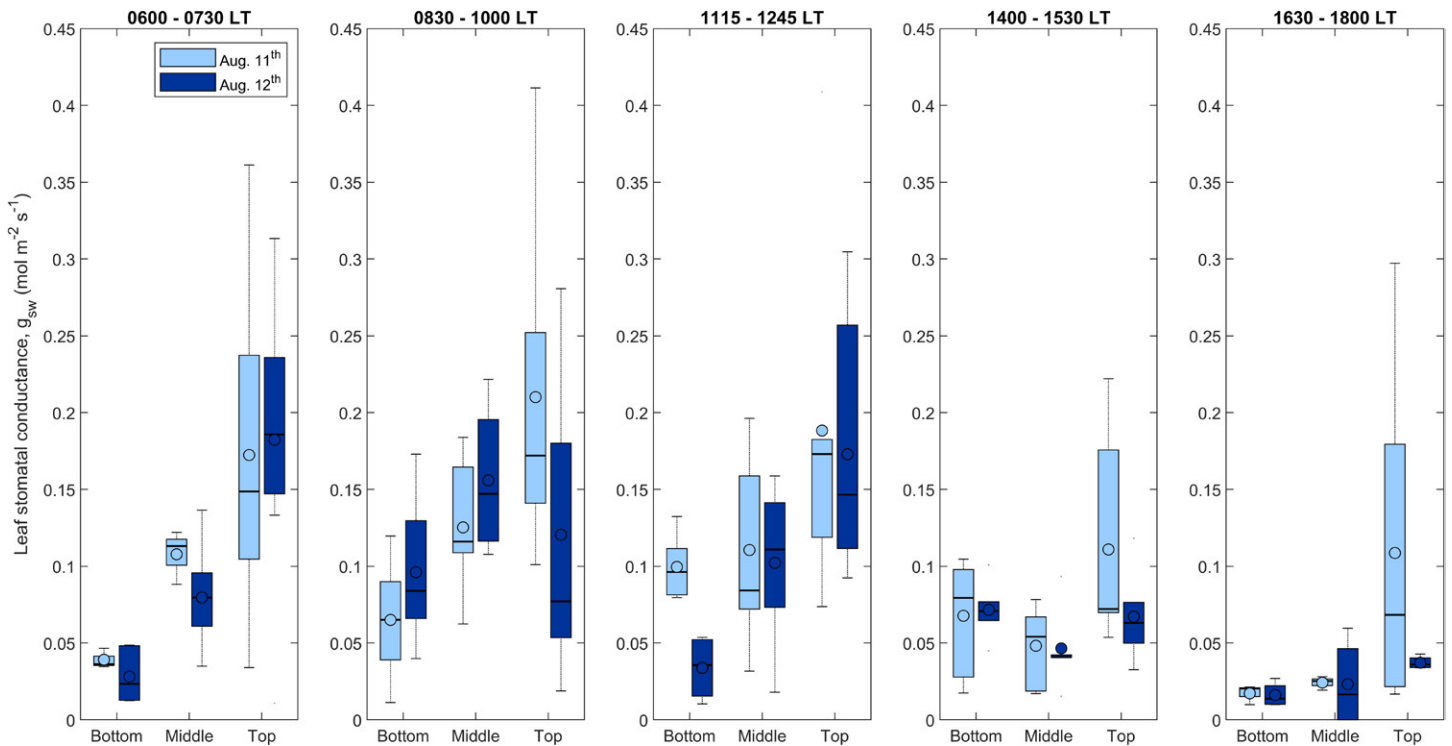

FIG. 3. Subdiurnal variability of the leaf stomatal conductance (g_{sw}) at different heights of the canopy collected during 11 and 12 Aug. Leaf samples (total 158 samples) were taken under sunlit (63 samples) and shaded (95) conditions at 3 heights: bottom (47), middle (50), and top (61). Leaf samples were taken from random trees. Canopy height is 40 m. Top samples were collected between 27 and 30 m. Medium samples were collected between 18 and 22 m. Bottom samples were collected at around 2 m. OBS were done using the LI6400XT instrument.

dependence is clearly observed on 11 August before midday with a linear pattern (intervals 0600–0730 LT and 0830–1100 LT) or more logarithmic (1115–1245 LT), with values that roughly increase by factor two between the bottom and middle and the middle and top. This dependency changes owing to the appearance of clouds in the afternoon which leads to similar values in the middle and bottom levels due to the simultaneous decrease of direct irradiance and the increased penetration of diffuse radiation (not measured during CloudRoots-Amazon22). This change in the partitioning of direct versus diffuse might be also dependent on the irradiance wavelength (Durand et al. 2021). As shown in Fig. 2, the lower averaged values of the global irradiance during the afternoon 12 August lead to lower leaf conductivity at the top of the canopy due to the presence of clouds. Appendix C shows the cloud depth observed by a cloud radar at the Campina site during both days. During 11 August, the cloud depth was always below 1 km, whereas during 12 August, cloud depths above 1 km were observed during the intervals 1115–1245 and 1630–1800 LT. These radiation and stomatal conductance observations need to be combined with temperature and water vapor deficit profiles as well as stable isotopologues of CO_2 and H_2O to determine the variation of soil and photosynthesis rate within the canopy.

4. Canopy-level processes: Carbon and water fluxes at the forest and atmosphere interface

To upscale measurements from leaf to canopy level, it is important to discriminate the individual contributions of soil and plant leaves and relate them to the canopy architecture. Environmental variables such as the transfer of radiation and the effects of vertical and horizontal turbulent transport also need to be taken into account. Measurements of the stable isotopologues of CO_2 and H_2O enable us to quantify the contributions of photosynthetic assimilation and respiratory components to NEE (Bowling et al. 2001) and of plant transpiration and soil evaporation to net evaporation (Rothfuss et al. 2012; Xiao et al. 2018). Within CloudRoots-Amazon22, three stable isotopologues' measurement techniques and strategies were used: gradient observations measured by continuous profiling measurements, discrete flask sampling profiles (2 days), and high-frequency observations (see appendix A).

a. Gradients of stable isotopologues in and above the canopy. We have measured the gradients and fluxes of CO_2, H_2O, and their abundant and scarce isotopologues. Figure 4 shows the diurnal variability of CO_2 and H_2O and their isotopic compositions, δ^{13}C-CO_2 and δ^{18}O-H_2O, for a diurnally aggregated period of 2 or 4 days (17–18 August or 15–18 August). Note these isotopic compositions reflect the ratio of measured scarce (heavy-element-bearing molecules) to abundant (light-element-bearing molecules) isotopologue mixing ratios, e.g., ^{13}C^{16}O$_2$/^{12}C^{16}O$_2$, relative to the ratio of the heavy to light isotope in the reference standard. A positive δ value means that the sample contains more of the heavy isotope than the reference standard; a negative δ value means that the sample contains less of the heavy isotope than the reference standard. Plant and soil exchange with the atmosphere is characterized by different relationships between abundant and scarce isotopologues, which can be used to identify the sources and sinks of CO_2 and H_2O in and above the canopy.

The depicted days were selected as an example of shallow-to-deep convection (15 and 16 August) and two consecutive shallow convection days (Table 2). The diurnal variability showed a shift in stability from the nocturnal, thermodynamically stable and characterized by gradients, to the diurnal (unstable) conditions at 0900 LT (1300 UTC). From this time and until 2000 LT, the four stable isotopologues show very similar patterns, i.e., the time series of all heights collapse to a single evolution, which indicates that they are well-mixed profiles above the canopy. This pattern is also followed by the 79-m discrete flask observations.
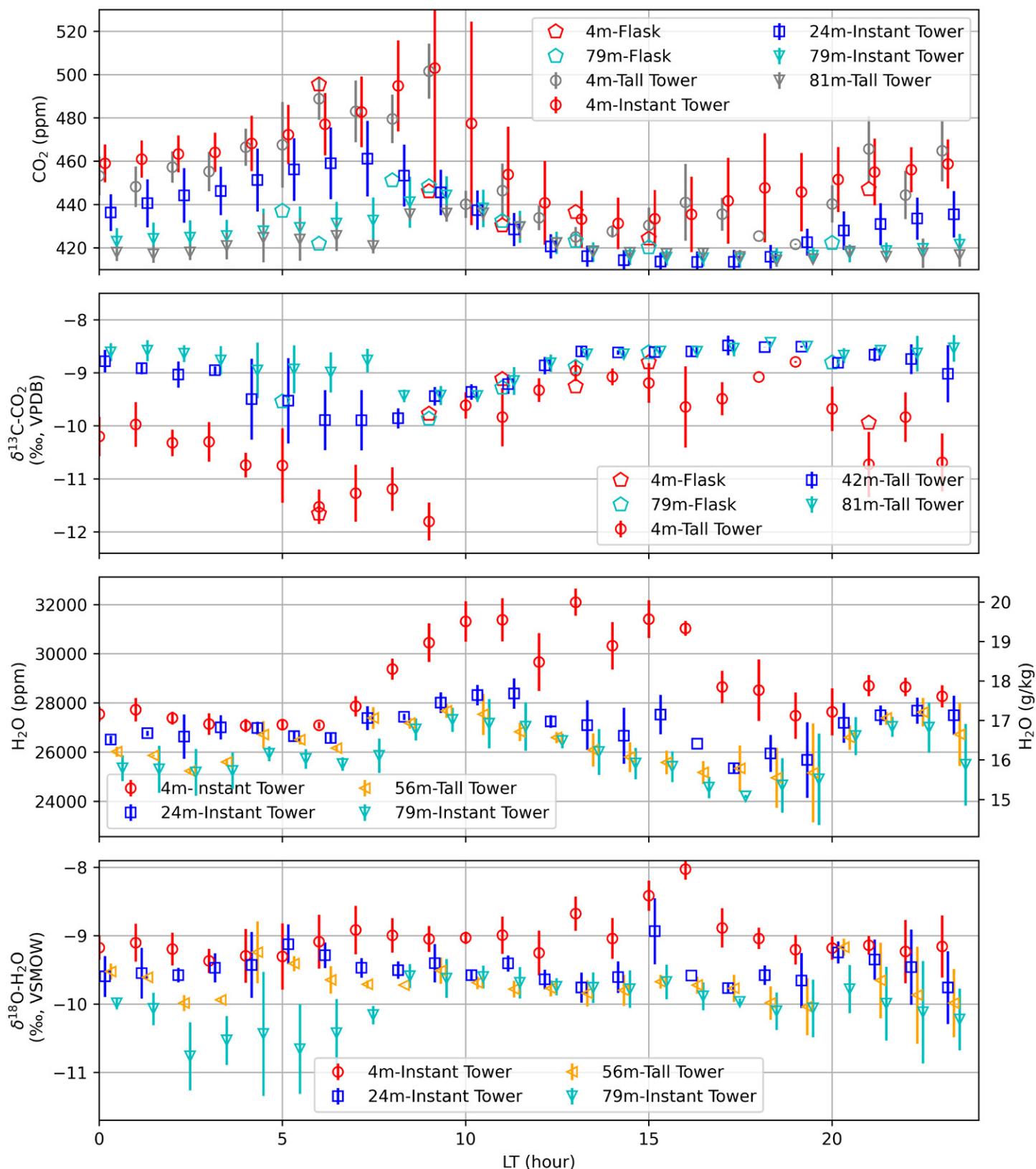
FIG. 4. Diurnal cycles of CO_2, $\delta^{13}C$-CO_2, H_2O, and $\delta^{18}O$-H_2O. (first row) Averaged CO_2 mixing ratio measured at the INSTANT tower by the Picarro G2401. Simultaneously measured tall tower CO_2 molar fractions (measured by the FTIR Spectronus analyzer) are shown in gray. (second row) Averaged δ $C^{13}CO_2$ values measured at the tall tower by using the FTIR Spectronus analyzer. (third row) H_2O concentrations and (fourth row) $\delta^{18}O$-H_2O values as measured at the INSTANT tower by the Picarro L2140-i and by the L2130-i at the ATTO tower (56 m). OBS of CO_2 and $\delta^{13}C$-CO_2 (top two panels) were taken on 15–18 Aug, and the OBS of H_2O and $\delta^{18}O$-H_2O were taken on 17–18 Aug. To complete the dataset, flask measurements of CO_2 and $\delta^{13}C$-CO_2 taken on 15 Aug are included. Details on the instrumentation can be found in appendix A.

This shows that turbulence, above the canopy, is efficiently mixing and able to partially penetrate, mix, and transport air from the different heights of the canopy (from 24 m and higher) into the ABL. Here, it is important to mention that the diurnal variability is controlled not only by canopy processes but also by nonlocal processes such as the entrainment of air masses from the residual layer into the free troposphere as shown by previous studies on CO_2 (Vilà-Guerau de Arellano et al. 2004; Patton et al. 2016) and stable isotopologues (Welp et al. 2012). The analysis of changes in the isotopologue composition variability measured during the campaign can therefore enable us to disentangle the contribution of local and regional sources of evaporation and the net ecosystem exchange in the Amazon basin, as indicated by Griffis et al. (2016).

The exception is the lower measurement height at 4 m, for both continuous and flask measurements. As shown in Fig. 4, at this level close to the ground, all the four components are decoupled from the evolution of the compounds measured at the other heights. This decoupling is driven by the more thermodynamically stratified mixing conditions in the middle of the canopy (not shown). In addition, there is a shift from CO_2 photosynthesis assimilation in the canopy top to the soil CO_2 respiration dominant conditions. Therefore, soil CO_2 efflux and soil evaporation are larger contributors, as also shown by the high CO_2 concentrations, and depleted $\delta^{13}CO_2$ values, indicating a source value of −28.3‰. Our objective here is to assess if these stable isotopologues measurements can help to quantify more accurately the flux partitioning between overstory and understory (Misson et al. 2007). For tropical rain forest, sources originated at the understory ET contribute 23.6% to the net ET (Jiménez-Rodríguez et al. 2020). To our knowledge, no previous study has identified the understory contribution to gross primary production, autotrophic and heterotrophic respiration, and net evaporation in the Amazon rain forest. Within CloudRoots-Amazon22, these high-precision measurements of CO_2 and H_2O, and their isotopic composition, characterized by distinct subdiurnal patterns for all components and heights, as shown in Fig. 4, will permit the use of Keeling plot techniques on different temporal and spatial scales. This analysis will provide a detailed and in-depth partitioning of NEE and ET (soil vs plants) and its dependence on environmental variables (Bowling et al. 2001; Pataki et al. 2003; Knohl and Buchmann 2005; Zhang et al. 2006).

b. Ejection and sweeping motions of stable isotopologues above the canopy.
High-frequency observations of CO_2 and H_2O complete the on-site gradient measurements of the isotopologues of CO_2 and H_2O. They enable us to study the role of turbulent dynamics (gust penetration into the canopy) of CO_2 and H_2O exchange (Fitzjarrald et al. 1988). The quadrant plot in Fig. 5 depicts the sweeping penetrative motions of air from the boundary layer into the canopy (Q3 quadrants with downdrafts quantified by $w' < 0$, shown at the two lower panels) and upward ejections of air masses (quadrants Q1 and Q2 characterized by $w' > 0$, shown at the two upper panels) originating from within the canopy. All these high-frequency measurements were taken at 56 m. This height is approximately 16 m above the canopy, and we consider it a representative level of the processes occurring at the interface between the canopy and the atmosphere, i.e., the roughness sublayer.

This plot shows 18 000 observations of the perturbations in CO_2' and H_2O' molar fractions and $\delta^{18}O\text{-}CO_2$ measured at 10 Hz over a 30-min time window from 1200 to 1230 LT (18 August). These perturbations are calculated using a Reynolds decomposition using $\phi' = \phi - \overline{\phi}$, where ϕ is the generic measurement and $\overline{\phi}$ is its average during the 30-min interval. The two main modes of exchange during this midday period are observed between the lower left quadrant Q3 in Fig. 5 (downdraft motions entering the canopy) and the upper-right quadrant Q1 (updraft motions from the canopy into the atmosphere). Here, we follow the quadrant analysis

criteria as suggested by Shaw et al. (1983). Downward moving air (inward transport) in Q3 (72% motions characterized by $w' < 0$) contain air parcels characterized by high CO_2 concentrations (positive fluctuation with respect to the 30-min average period) and by low in H_2O concentrations. These air parcels likely originate from the convective boundary layer dynamics. They are characterized by an ABL signal indicating the transport, by subsiding motions, of air masses rich in CO_2 and dry air originated and entrained from the free tropospheric air (Welp et al. 2012; Griffis et al. 2016). We interpreted values around 41.3‰ as air masses characterized by background isotopic composition of $\delta^{18}O$-CO_2 in the local ABL. In contrast, air parcels in Q1 were ejected from the canopy (68% characterized by $w' < 0$). Canopy

Fig. 5. Quadrant plot of HF perturbations in CO_2 and H_2O, colored with 10-Hz $\delta^{18}O$-CO_2 measurements from an Aerodyne TILDAS-CS. The 30-min time interval started at 1200 LT 18 Aug 2022 and was measured at 57 m on the ATTO tower. Canopy height is 40 m. Quadrants are defined in terms of positive and negative fluctuations of vertical velocity w': Q1 is the outward transport from the canopy into atmosphere, Q2 corresponds to ejections from the understory, and Q3 corresponds to the inward transport from the atmosphere into the canopy. The percentages correspond to the fluctuation vertical velocity per quadrant. Details on the instrumentation can be found in appendix A.

outward transport motions are characterized by reduced levels of CO_2 and increased H_2O reflecting active vegetation processes with high rates of photosynthesis and transpiration occurring at around midday (Fig. 3). Strongly enriched $\delta^{18}O$-CO_2 signals (>41.6‰) confirm leaf contact since CO_2 oxygen isotopes exchange rapidly with isotopically enriched leaf water in the presence of carbonic anhydrase (CA) (Yakir et al. 1994; Adnew et al. 2020). The Q2 quadrant provides intriguing evidence of air parcels predominantly influenced by the most dominant soil signal. We find that ejection motions of air parcels are less frequent with increasing CO_2 and H_2O contents as was also reported by Thomas et al. (2008). We associate their upward transport with energetic canopy-scale eddies that are able to penetrate almost unperturbed into the canopy down to the understory transporting air with high levels of H_2O and CO_2 back to sensor height (56 m) above the canopy.

c. One-min turbulent fluxes in relation to cloud radiation perturbations.
Using the data of CloudRoots-Amazon22, we plan to calculate isofluxes (Griffis 2013) using two different observational techniques: the eddy covariance (Wehr et al. 2013) and the DBLS scintillometer (van Kesteren et al. 2013). As a preparatory example, Fig. 6 shows how the sensible heat flux (H) varies due to the PAR fluctuations. Magnitude and duration of the fluctuations depend on cloud passage and the thickness of the cloud. The high-frequency fluctuations in global horizontal irradiance, proportional to PAR (Fig. 2), drive fluctuations in the canopy turbulent fluxes at comparable time scales (Kivalov and Fitzjarrald 2019; Vilà-Guerau de Arellano et al. 2023), as highlighted by the 1-min observations of the DBLS technique (van Kesteren et al. 2013). These collocated radiation−H fluctuations are with some time lag with respect to PAR which indicates that radiation is not the only driver but also other processes regulating the exchange (stomatal conductance, turbulence) play a role in controlling the sensible heat flux. As shown in Fig. 6, this variability is not registered (filtered out) in the
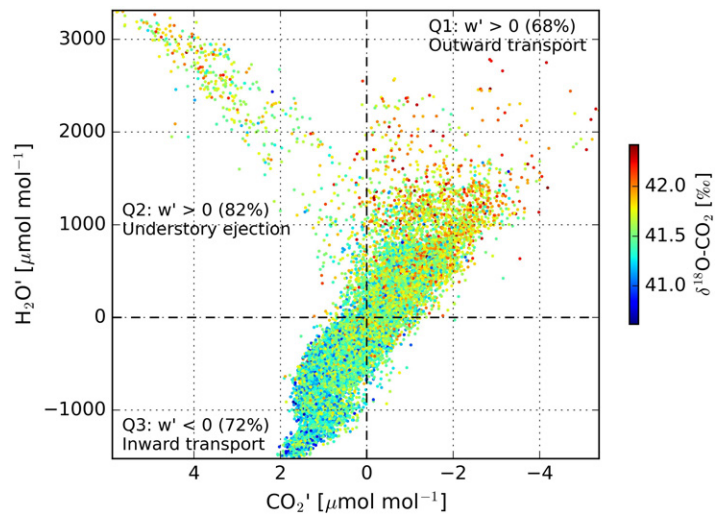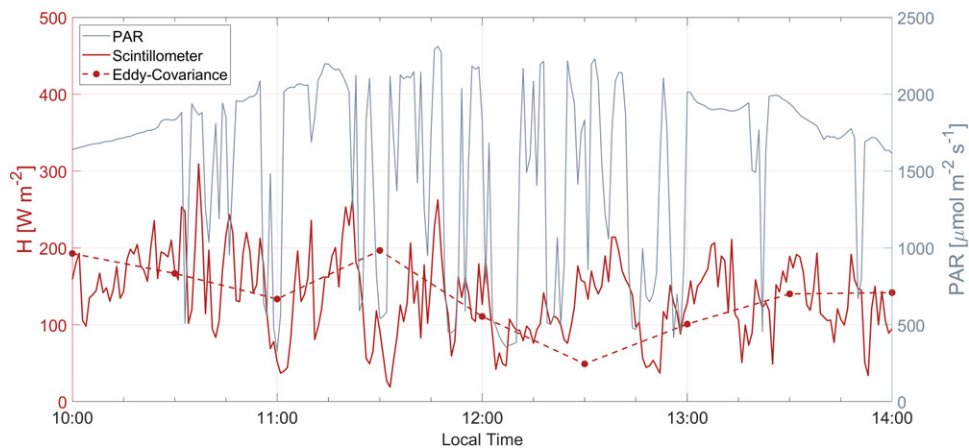
Fig. 6. Collocated OBS of PAR (black) and sensible heat flux (*H*) taken during August 2022. The red dots connected with the line show the standard 30-min average by EC, and the dark red line shows the 1-min averages determined using the displaced-beam laser scintillometer. The cumulative values (the 4-h interval under analysis, from 1000 to 1400 LT) of *H* for EC and scintillometer are equal so as to better highlight the dynamic differences. This day is categorized as a ShCu day (Table 2).

standard 30-min average eddy covariance observations. These advanced measurements of canopy turbulent fluxes will enable us to study how the vegetation responds to these rapid variable cloud radiation perturbations of varying intensity. Note that the scintillometer technique, unlike eddy covariances, does not rely on integration over all eddy scales that contribute to the turbulent transport. Rather, it determines turbulence variables, structure parameters of temperature, and dissipation rate of the turbulent kinetic energy on eddy scales that lie in the inertial range of the refractive index spectrum, which are linked to fluxes using MOST. The disadvantage of the technique is that it is more indirect because it relies on inertial range behavior of the observed eddies and the assumption that MOST holds. Both assumptions will require to be further investigated.

5. Cloud-level processes
a. Clear-to-cloudy profiles: Diurnal evolution. Ejection and sweeping motions at the forest–atmosphere interface regulate the exchange of energy, water, and carbon dioxide. These motions are also influenced by ABL-scale structures that can lead to changes in the turbulent fluxes at the top of the canopy (Patton et al. 2016). Therefore, to connect these canopy fluxes to the vertical distribution of the ABL state variables, we measured the morning and afternoon profiles of potential temperature (θ), specific humidity (q), and carbon dioxide (CO_2). Figure 7 shows the observed profiles collected during the afternoon of 18 August (period 1400–1800 LT) characterized by shallow cumulus. The figure combines observations from the two tall towers, the sounding (potential temperature and specific humidity), and aircraft vertical profiles (H_2O and CO_2) (Table 1). In the bottom panels, we show the first 500 m, which are dominated by large gradients which even change sign in and above the canopy of potential temperature and carbon dioxide. The observations show the large differences in profiles in and above the canopy with respect to magnitude and gradients. The large differences in values are the largest for CO_2: 431 ppm at the lowest level, 414 ppm near the canopy top, and 419 ppm within the well-mixed ABL. These data can contribute to the current debate on the impact of canopy on the inertial and roughness layer at the Amazon rain forest (Dias-Júnior et al. 2019). They also provide observational evidence to evaluate the effects of the canopy turbulence on the mean flux profiles (Harman 2012), i.e., modifications of MOST, which require to be implemented in numerical weather and global climate models (Bonan et al. 2021).
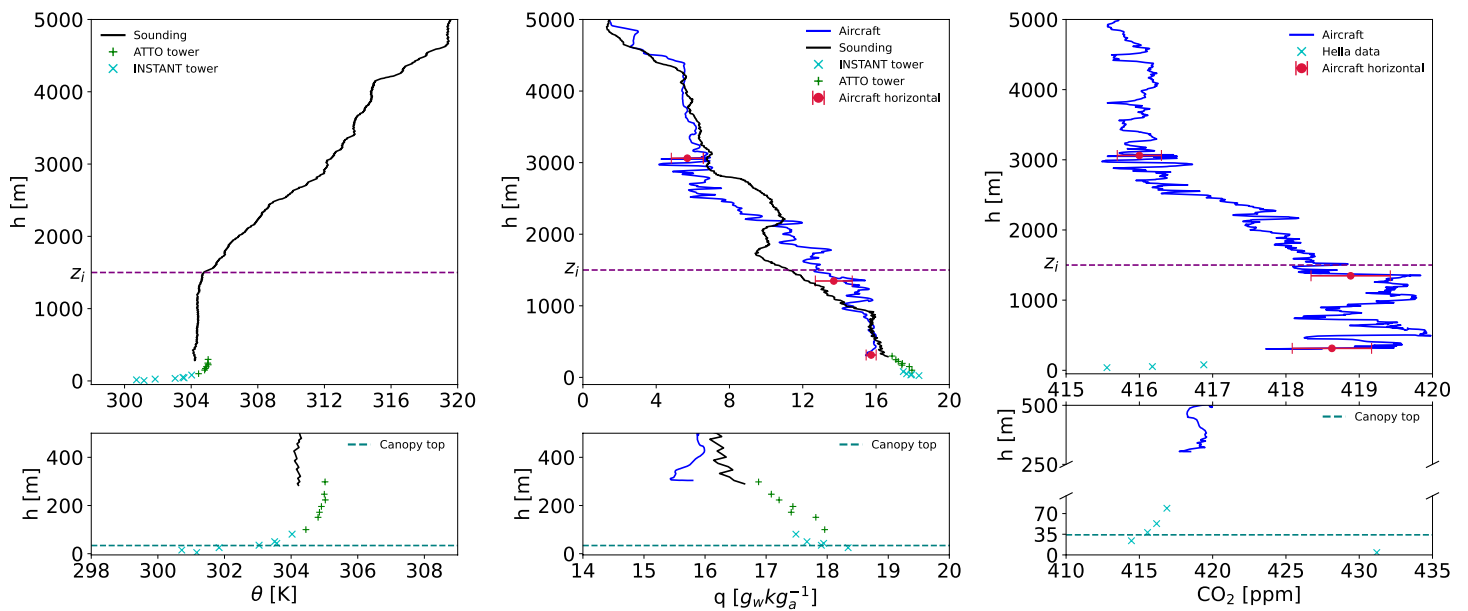
Fɪɢ. 7. Vertical profiles of (left) potential temperature, (middle) specific humidity, and (right) carbon dioxide measured on 18 Aug during the afternoon: potential temperature 1800 LT (2200 UTC), specific humidity 1400 LT (1800 UTC), and carbon dioxide 1400 LT (1800 UTC). The height h (y axis) is in meters above sea level. The figure includes the following OBS taken at/by INSTANT and ATTO tall towers (all variables), aircraft profiles, and mean and standard deviation of the horizontal raster (specific moisture and carbon dioxide) and radio soundings (potential temperature and specific humidity). The ABL height is indicated by z_i.

In the upper panels, which display the altitude from the top of the forest up to 5000 m, we find that the three variables very closely follow a three-layer structure determined by a subcloud layer (that is well-mixed for the three conserved variables below 1500 m), a cloud layer (that is conditionally unstable from 1500 to 3000 m), and the free troposphere (that is thermodynamic stably stratified > 3000 m). This three-layer structure is already present in the morning profiles (0900–1100 LT) of the three variables (see appendix D and Fig. B1) but now with an ABL depth at 1000 m. These soundings indicate that the diurnal growth of the ABL (subcloud layer) is between 0.03 m s⁻¹ (108 m h⁻¹) and 0.05 m s⁻¹ (180 m h⁻¹) (see Fig. E1). The transport in the subcloud layer is mainly driven by turbulence depending on the partitioning between sensible and latent heat fluxes at the canopy top. At the cloud base, the transport from the subcloud layer into the cloud layer, namely, the mass flux (M) or ventilation, is driven by two processes: at the canopy level by the partition of the turbulent fluxes, which is partly controlled by plants (Sikma and Vilà-Guerau de Arellano 2019), and, at the cloud scale, by the thermodynamic conditions at the ABL and cloud, more specifically the dynamic conditions at their interface, and the role of the temperature and specific humidity lapse rates (van Stratum et al. 2014). It has been shown numerically that this mass flux is important for the transport of atmospheric compounds such as isoprene between the subcloud and cloud layers (Ouwersloot et al. 2013). Compared to present conditions, mass flux is modified under conditions of enhanced CO₂ levels and warming (Sikma et al. 2019).

b. Cloud characteristics: Cloud core and mass flux. As a representative example of the advantages to gather collocated and comprehensive observations to study cause–effect relationship between canopy and cloud processes, Fig. 8 shows the observed and modeled calculations of the cloud core area fraction a_{cc} and the mass flux M. Both variables are calculated for the aggregated days characterized by shallow (ShCu) and deep (ShDeep) convection, respectively. The a_{cc} is defined as the region at cloud base in which the air parcels are positively buoyant and therefore move upward with a velocity. Note that a_{cc} is related to the cloud cover, but it has smaller values. We calculate a_{cc} and M based on a parameterization derived by Neggers et al. (2006) and van Stratum et al. (2014). It was
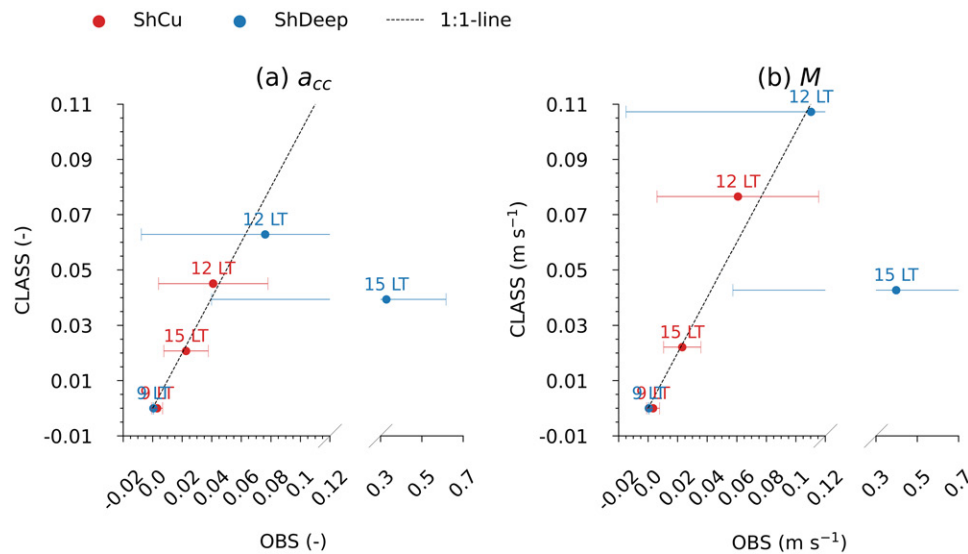
FIG. 8. (a) Area fraction of cloud core a_{cc} and (b) mass flux M. The calculations are based on OBS (x axis) and the coupled rain forest–atmosphere (CLASS) (y axis). They correspond to 6-day aggregated of ShCu and 4-day aggregated of ShDeep convection, based on the classification presented in Table 2. Based on the means of these aggregated days, we calculate the standard deviation and present as the range of variability. The complete derivation of the calculation is presented at appendix E. This appendix also shows the six intermediate variable calculations (see Fig. E1) needed for the calculations of a_{cc} and M.

further revised and improved with a suite of large-eddy simulations numerical experiments on marine and land shallow cumulus by van Stratum et al. (2014) and Sikma and Ouwersloot (2015). The formulae used to calculate these two cloud properties as well as the intermediate variables are explained, and their results are shown in appendix E. In Fig. 8, the parameterization [Eq. (E4)] is calculated using two different input variables: tower/sounding observations (OBS) and model calculations (CLASS) using a land–atmosphere model that include cloud cover and mass flux representations (van Stratum et al. 2014). The numerical experiments reproduce the aggregated of the ShCu and ShDeep observational situations, using initial and boundary conditions constrained by the observations.

Within the CloudRoots-Amazon22 objectives, the analysis of these two variables is a key element to show the causality of canopy-cloud processes. In short, air parcels move upward with a convective velocity that depends on the heat and moisture flux at the canopy top, i.e., buoyancy (see Fig. E1a) regulated by the canopy conditions. The area fraction of the cloud core [Eq. (E4) in appendix E] is proportional to the atmospheric boundary layer growth and the differences in moisture content between the free troposphere and the mixed-layer values, represented by the jump of the specific humidity at the cloud base. This parameterization is inversely proportional to the transition layer (Δz). It therefore separates the regimes of cloud moist convection [quantified by lifting condensation level (LCL)] from those of dry convection and mechanical mixing below (quantified by h) (Augstein et al. 1974; Albrecht et al. 1979). As such, this representation integrates processes driven by the canopy fluxes to ABL dynamic processes.

As shown in Fig. 8, there is a satisfactory agreement between a_{cc} and M inferred from the observations and from the calculations using CLASS. The outlier is the value for ShDeep at 1500 LT which indicates that under deep convective conditions, the assumptions included to derive Eq. (E4) are probably no longer valid. At 1200 LT, and for ShDeep, the higher values a_{cc} and M indicate the more favorable conditions to initiate deep convection. However, we need to be cautious about our analysis since the differences in the intermediate variables are minimal and subtle as shown in Fig. E1. Here, we take as a representative example of the

variability in the calculation of Δz (Fig. E1c). We interpret $\Delta z < 0$ as a local condition that favors the formation and intensification of cloud: air parcels released at the canopy top have more favorable conditions to reach condensation. We calculate LCL from the soundings as the height where and air parcel has reached the relative humidity 100%. The h is calculated as the maximum of the potential temperature gradient in between 300 and 2000 m following the definition by Sullivan et al. (1998). For the key hours of the potential intensification and transition of convection, all the values are ranging between −100 and 100 m indicating the high variability of the calculations, both in observations and conceptual modeling.

6. Future perspectives

How are surface and atmospheric processes coupled to control moist, shallow and deep convection (Gentine et al. 2013) and what is the influence of local processes on cloudy boundary layer dynamics (Vilà-Guerau de Arellano et al. 2023)? Recent studies have described key processes related to these questions: the role of vertical wind shear (Drueke et al. 2021; Cecchini et al. 2022), the role of fog (Anber et al. 2015) and low-level jets (Henkes et al. 2021) during the morning transition, and the impact of weather on aerosol distribution (Machado et al. 2021) in the Amazon region. The latter aspect is discussed by Gentine et al. (2019) who stressed the need to integrate regional and large-scale changes in ocean to land flow and the inland distance of penetration influencing local coupling, i.e., moisture recycling and changes on aerosol properties (Zemp et al. 2014).

Our modeling strategy, constrained and evaluated by the campaign data, aims to contribute to this debate by explicitly resolving radiation transfer, turbulent eddies, and cloud dynamics using large-eddy simulations (LESs) (Heus et al. 2010; Ouwersloot et al. 2017). Here, the strategy is two-fold: (i) coupled to dynamic representations of explicit canopy vegetation responses to ABL and cloud evolution (Patton et al. 2016; Pedruzo-Bagazgoitia et al. 2023) and (ii) including the radiation effects of cloud shading (Lohou and Patton 2014; Horn et al. 2015) and the three-dimensional effects of radiation at the surface (Veerman et al. 2020). Key in our approach is to integrate a complete dataset of isotopologues and isofluxes to advance in the determination of the sink and sources of carbon and water (Lee et al. 2012). Here, we follow the recommendations of Bonan et al. (2021) to make use of multilayer canopy models coupled to atmospheric processes to advance our understanding of the forest–atmosphere interactions. These detailed LES experiments are supported by the conceptual coupled forest–atmosphere model CLASS (Vilà-Guerau de Arellano et al. 2015) in which clouds (van Stratum et al. 2014; Cecchini et al. 2022), the land surface (van Heerwaarden and Teuling 2014), and the carbon cycle (Vilà-Guerau de Arellano et al. 2012) that includes the diurnal variability of CO_2 and H_2O stable isotopologues (Vilà-Guerau de Arellano et al. 2019) are simultaneously solved.

As shown in Figs. 8 and E1, numerical experiments using a conceptual model such as CLASS, supported by observations and LES numerical experiments, can be viewed as a surrogate of a typical weather or climate grid cell. In this particular case, CLASS model results compared to observations enable us to determine key aspects of the mass flux parameterizations (Neggers et al. 2006; van Stratum et al. 2014) or to determine the level of coupling between local processes and nonlocal processes such as entertainment, subsidence, and advection (Mangan et al. 2023; Aguirre-Correa et al. 2023). By combining the analysis of processes with the CloudRoots-Amazon22 dataset, we can attempt to reduce the uncertainties around the estimation of atmospheric boundary layer depth as presented in the reanalysis of ERA5 (Dias-Júnior et al. 2022). In our modeling approach, the contribution of regional processes to the diurnal variability, for instance, by long-range transport of moisture and carbon dioxide from remote sources, on canopy fluxes and clouds are simultaneously solved as part of a continuum using the ECMWF-IFS to provide model boundary conditions

(Boussetta et al. 2013). This regional perspective will enable us to determine and distinguish the origin of air masses in which moisture is recycled (Trenberth 1999; Rösner et al. 2018) and quantify potential effects on atmospheric moisture recycling through vegetation (Staal et al. 2018). With respect to CO_2, and in combination with atmospheric transport models (Botía et al. 2022), it will enable us to improve the quantification of the contribution of upwind air masses on the local diurnal CO_2 cycle.

7. Summary

The CloudRoots-Amazon22 campaign generated a comprehensive, high-frequency, 2-week dataset that simultaneously probes (micro) meteorology, including cloud properties, and soil/plant dynamics relating to atmospheric composition in and above the pristine rain forest. Collocated surface and upper atmospheric observations were taken around the supersites of ATTO and Campina in August 2022 (Southern Hemisphere Amazon dry season). These data provide unique constraints for modeling important uncertainties regarding evaporation/precipitation and sources/sinks of CO_2 in the Amazon basin, connecting local processes to large-scale circulations at the diurnal scale. Our main findings are as follows:

1) Our leaf-to-canopy observations confirmed that there is an asymmetry in the stomatal conductance and subsequent fluxes of water, carbon, and energy, with more favorable conditions in the morning compared to the afternoon. This asymmetry is strongly regulated by light fluctuations (order seconds to minutes) driven by clouds and in-canopy penetration.

2) Slow/fast and accurate measurements of CO_2 and H_2O stable isotopologues combined with high-frequency turbulence measurements enable us to determine CO_2 and H_2O sources and sinks at the over- and understory. The analysis shows that thermal stratification in and above the canopy controls mixing and transport. In intermittent situations, turbulence is able to penetrate to the bottom of the canopy shown by different signals of $\delta^{18}O\text{-}CO_2$. Quadrant analysis shows how sweeping and ejection motions transport CO_2-rich/poor and dry/moist air masses between the boundary layer and the canopy.

3) One-min turbulent fluxes inferred by scintillometer observations show large fluctuations related to the radiation and transport perturbations related to the passage of clouds.

4) We find a similar and consistent vertical structure of potential temperature, specific humidity, and carbon dioxide characterized by a well-mixed subcloud layer and a cloud layer. This pattern occurs not only in shallow cumulus cases but also in days in which the transition shallow-to-deep occurs. In both cases, we calculate two metrics that connect canopy to cloud processes: the area fraction of the cloud core and the mass flux that vents subcloud properties to the cloud layer. Our observations, supported by results using conceptual modeling results, show that these cycles are characterized by a strong subdiurnal variability, with favorable conditions for the formation of boundary layer clouds in the afternoon.

The data collected during the CloudRoots-Amazon22 campaign will provide novel opportunities to connect processes at leaf, canopy, and cloud levels. Placing CloudRoots-Amazon22 in a broader framework, this field campaign complements and adds a comprehensive observational perspective to the coupling between evaporation and clouds (Findell et al. 2011; Taylor et al. 2011) by adding the active role played by plants. Our approach also introduces a well-resolved local perspective on top-down regional–global studies in which vegetation responses are investigated in the context of clouds (Doutriaux-Boucher et al. 2009; Pietschnig et al. 2021; Park et al. 2021).

APPENDIX A
Isotopologue Measurements

CloudRoots-Amazon22 campaign bolstered seven distinct setups, all measuring unique aspects of the CO_2 and H_2O isotopic budget. Tables A1 and A2 provide a detailed overview of these various setups, which are categorized into continuous profile (PF) measurements, high-frequency (HF) observations to calculate isofluxes, and discrete flask (DF) measurements. Continuous profile measurements were carried out by the Max Planck Institute for Biogeochemistry team at several sampling heights in and above canopy by using multiple inlet lines that sample sequentially through custom-made inlet manifolds. The analyzers

TABLE A1. CO_2 isotope instrument specifications.

	LS-CO_2 PF	LS-CO_2 HF	FTIR PF	Air samples DF (MPI and IMAU)
Manufacturer	Picarro	Aerodyne	ACOEM	Thermo Fisher
Model	G2401	TILDAS-CS	Spectronus	MAT252 IRMS
Species	CO_2 (CO, H_2O, and CH_4)	CO_2, $\delta^{13}C$, and $\delta^{18}O$	CO_2 and $\delta^{13}C$ (CH_4, CO, and N_2O)	CO_2, $\delta^{13}C$, $\delta^{18}O$, and $\delta^{17}O$ (etc.)
Sampling frequency	Profile in 15 min	10 Hz	Profile in 1 h	Profile in 2 h
Described in	Winderlich et al. (2010)	Moonen et al. (2023)	van Asperen et al. (2023)	Adnew et al. (2022), Werner et al. (2001)
Location	INSTANT	ATTO	ATTO	ATTO and INSTANT
Inlet height(s) (m)	4, 24, and 79	56	4, 42, 81, 150, 273, and 321	4, 24, 38, 60, 80, and 321
Calibration approach	Flowthrough gaseous standard	Trapping gaseous standards	Flowthrough gaseous standard	Reference standard (gas)
Calibration types	Span	Span, mole-frac dependence	Span	Offset from standard
Operational (2022)	8–21 Aug	8–21 Aug	7–21 Aug	14, 15, 18 Aug

	LS-H$_2$O PF	LS-H$_2$O HF	Leaf/soil samples DF
Manufacturer	Picarro	Picarro	Thermo Fisher
Model	L-2140i	L-2130i (HF)	Delta^{PLUS} + XL IRMS
Species	H$_2$O, δD, δ^{18}O, δ^{17}O	H$_2$O, δD, δ^{18}O	δD, δ^{18}O (N, P, gs, etc.)
Sampling frequency	Profile in 24 min	4 Hz	178 samples in 2 days
Described in	Komiya et al. (2021)	Moonen et al. (2023)	Gehre et al. (2004)
Location	INSTANT	ATTO	INSTANT
Inlet height(s) (m)	4, 24, 38, and 79	56	−85, −45, −15, −5, 2, 19, and 30
Calibration approach	Vaporizing liquid standards[a]	Vaporizing liquid standards	HTC reactor, liquid standards
Calibration types	Span, mole-frac dependence	Span, mole-frac dependence	Span
Operational (2022)	14–21 Aug	8–21 Aug	14, 15 Aug

[a] LS-H$_2$O PF's isotope measurement values were cross-checked against the calibrated LS-H$_2$O HF's ones because LS-H$_2$O PF's calibration system was unfortunately not functional during the field campaign.

used for this purpose are placed in air-conditioned laboratories at the base of the towers. The high-frequency analyzers were placed in air-conditioned enclosures on the 54-m platform of the ATTO tall tower. They were used to infer isoflux measurements by combing them either with eddy covariance or the laser scintillometer. The short inlet line in combination with heated, smooth, inlet tubing, high gas flow rates, and adequate postprocessing minimized the effects of inlet line attenuation or lag (Moonen et al. 2023). Finally, leaf, air, and soil samples were collected during 2 days (14 and 15 August 2022) (Fig. 4) for isotopic analysis at the MPI Jena and the Institute for Marine and Atmospheric Research Utrecht (IMAU). The sampling was done in eight specific time windows (local times: 0500–0526, 0601–0621, 0802–0823, 0902–0926, 1103–1121, 1301–1327, 1501–1527, 2002–2055) and at 6 heights.

The vertical air sample profiles provide the backbone of the CO$_2$ isotopic composition measurements as they are highly accurate. Water isotopic compositions of leaf and soil samples should reveal the isotopic source compositions of evaporation and the net ecosystem exchange, i.e., soil versus plant. The δ^2H-H$_2$O and δ^{18}O-H$_2$O and CH$_4$ were measured on a Thermo Delta^{PLUS} + XL IRMS coupled to a high-temperature conversion (HTC) reactor via a ConFlo III. Two in-house water standards were tied to Vienna Standard Mean Ocean Water–Standard Light Antarctic Precipitation (VSMOW-SLAP) (Gehre et al. 2004). Leaf and soil (0–10, 10–20, 40–50, and 80–90 cm) waters are obtained by cryogenic vacuum extraction.

LS-H$_2$O PFs' isotope measurement values were cross-checked against the calibrated LS-H$_2$O HF's ones because the LS-H$_2$O PFs calibration system was unfortunately not functional during the field campaign.

APPENDIX B
Profile Evolution of Biogenic Volatile Organic Compounds

Figure B1 shows the evolution of isoprene, the sum of methyl vinyl ketone (MVK) plus methacrolein (MACR) and isoprene hydroxyhydroperoxide (ISOPOOH), and the sum of monoterpenes measured on the consecutive days 15 and 17 August, at 3 heights in the ATTO tower: 80, 150, and 320 m. All species are detected by a proton transfer reaction time-of-flight mass spectrometer (PTR-ToF-MS) (Ionicon Analytik, Innsbruck, Austria) using 3/8-in. OD insulated Teflon lines to connect to the respective sampling height. The five compounds follow a clear diurnal variability governed by the diurnal emission variability in BVOCs, oxidative chemistry, and the boundary layer dynamic evolution (Karl et al. 2009; Vilà-Guerau de Arellano et al. 2012). From the figure, we find that measurements at 150 and 320 m are more representative
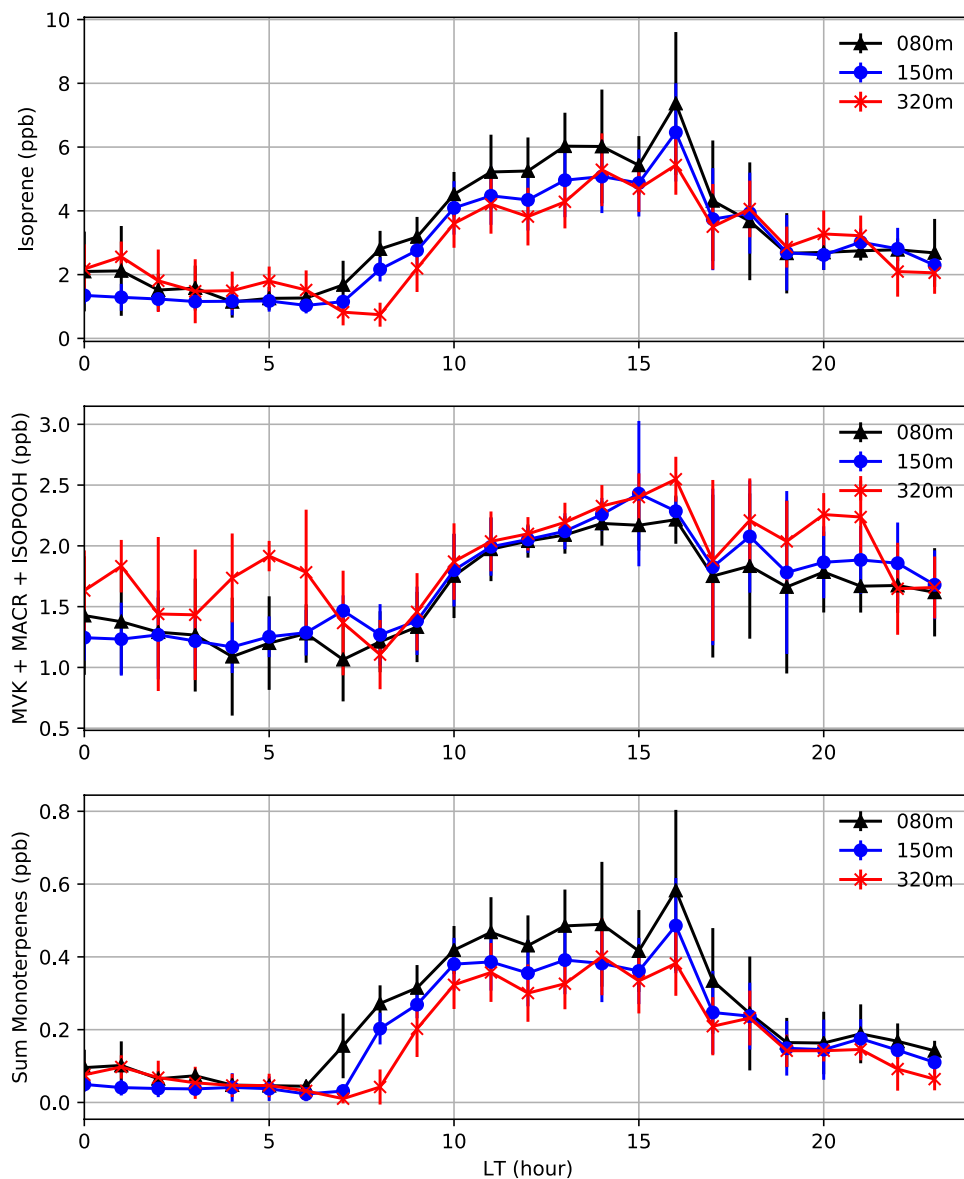
Fig. B1. Diurnal cycles of isoprene, the sum of MVK plus MACR and ISOPOOH, and the sum of monoterpene. (top) 1-h averaged isoprene mixing ratio. (middle) Averaged of the aggregate of MVK, MACR, and ISOOPOH mixing ratio. (bottom) Sum of monoterpenes mixing ratios. All OBS taken at the ATTO tower for the period 15 and 17 Aug 2022 are averaged over this period. Error bars show the standard deviation.

of the atmospheric boundary layer during the day. This can be seen by their collapse in one single line due to the well-mixed convective conditions as shown in Fig. 7, whereas the 80-m observations are still within the roughness sublayer (Harman 2012).

APPENDIX C
Evolution of Cloud Depths

Figure C1 shows the observed cloud depth/thickness organized in five temporal periods (similar to Fig. 3) during 11 and 12 August 2022. The observations were taken with Doppler cloud radar MIRA. Vertical profiles of reflectivity every 5 s were taken. The retrieval algorithm analyzes the vertical profiles and considers the first real value (a hit in the cloud radar signal either a cloud or a rain droplet) to be the cloud base. Subsequently, it analyzes all the cloud/rain values in a column until it finds a value with no cloud/rain value. This is considered to be the cloud top. The code considers every continuous cluster of data to be a cloud, which

means that if the code detects a droplet at a given height z at time t, if in $t + 1$ it identifies a droplet at height z, $z + 1$, or $z - 1$, the code will consider these data to be components of the same cloud. Finally, the cloud thickness of a certain cloud is calculated according to the maximum height of the cloud top minus height of the cloud base.

APPENDIX D
Morning Profiles of Potential Temperature, Specific Humidity, and Carbon Dioxide

Figure D1 shows the observed profiles collected during the morning flight (during the period 0900–1100 LT). The figure combines observations from the two tall towers, the sounding (potential temperature and specific humidity), and aircraft profiling (H_2O and CO_2) (Table 1). The ABL depth is at 1000 m, and the three-layer structure as described in Fig. 7 subcloud layer (well mixed), cloudy boundary layer, and free troposphere layer is already well defined.

Fig. C1. Cloud thickness observed with the Doppler cloud radar MIRA during (top) 11 Aug and (bottom) 12 Aug. The OBS are clustered using the same periods as the ones of the OBS of the stomatal conductance (Fig. 3). Based on the number of hits in the radar signal, probability distribution functions are calculated for each interval.

APPENDIX E
Representations of Area Fraction Cloud Core and Mass Flux

To support Fig. 8, we present all the formulas and the intermediate variables in the calculation of the area fraction cloud core and mass flux. The formulation of the area fraction of the cloud core (a_{cc}, dimensionless units) and the mass flux (M, units of velocity) at cloud base are presented below. We define a_{cc} as the region of the upward vertical motions which are positive buoyantly within the cloud. The mass flux at the cloud base is defined as the upward velocity within a_{cc} which transports mass from the subcloud layer into the cloud layer. Following Betts (1973), the kinematic mass flux is defined by the area fraction of cloud cores a_{cc} multiplied by the difference between the cloud core vertical velocity (w_{cc}) and the domain-averaged vertical velocity at the cloud base ($\bar{w}_{cb}$):

$$M = a_{cc}\left(w_{cc} - \bar{w}_{cb}\right). \tag{E1}$$

Here, we will assume that $\bar{w}_{cb}$ is much smaller than w_{cc}, and therefore, we neglect it in Eq. (E1). Our objective to parameterize Eq. (E1) is two-fold: to calculate cloud characteristics by means of variables that were observed during CloudRoots-Amazon22 and
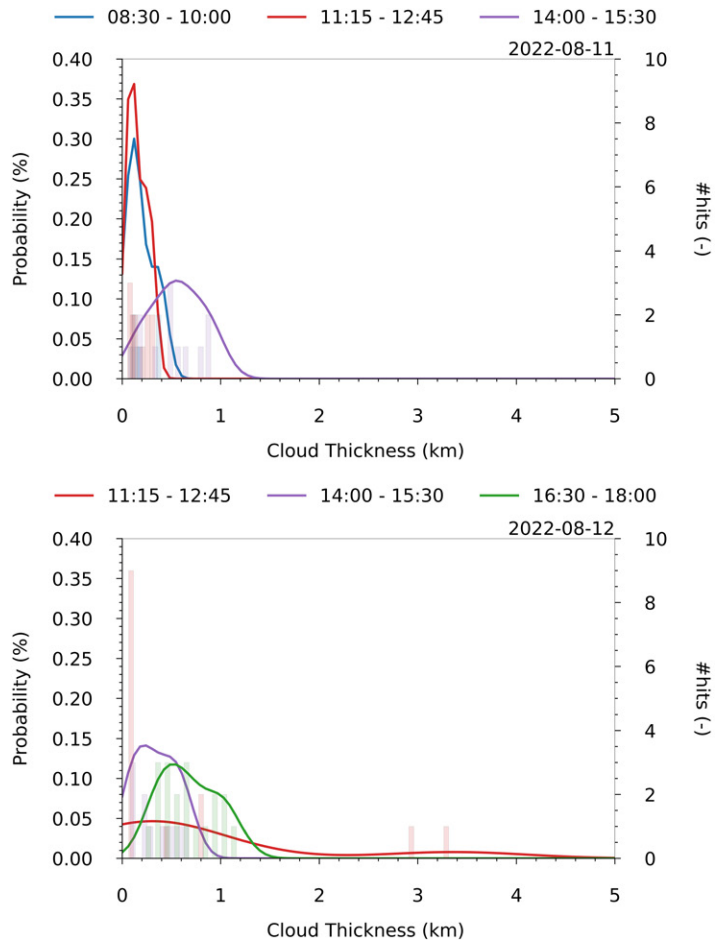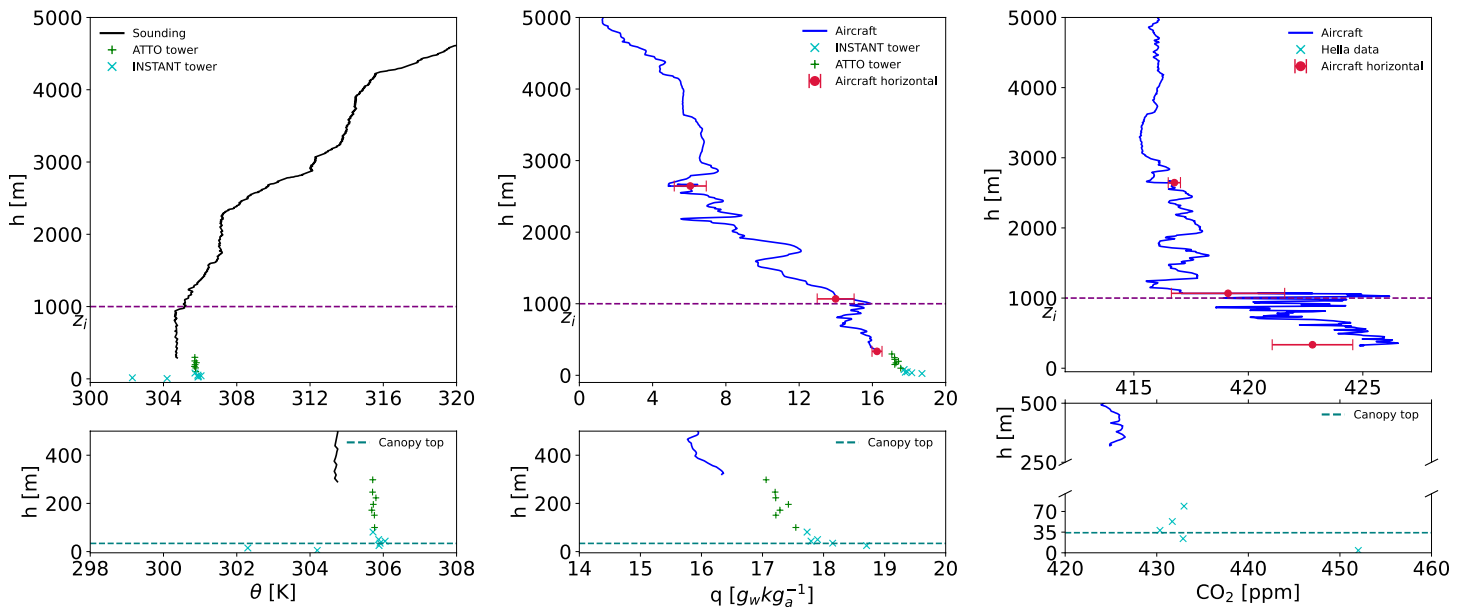
FIG. D1. Vertical profiles of (left) potential temperature, (middle) specific humidity, and (right) carbon dioxide measured 18 Aug 2022 during the morning: potential temperature 1500 LT (1100 UTC), specific humidity 1000 LT (1400 UTC), and carbon dioxide 1000 LT (1400 UTC). The height h is in meters above sea level, and the boundary layer z_i is marked by the dashed line. The figure includes the following OBS: INSTANT and ATTO tall towers (all variables), aircraft profiles and mean/standard deviation horizontal rasters (specific moisture and carbon dioxide), and radio soundings (potential temperature and specific humidity). The ABL height is indicated by z_i.

to determine by means of a conceptual land–atmosphere model which uses similar representations of area fraction cloud core and mass flux as weather and climate models and its level of representativeness. Therefore, it is useful to determine the relationships between surface processes and the dynamics of the boundary layer and cloud base as presented and discussed in Fig. 8.

Based on the original parameterizations proposed by Cuijpers and Bechtold (1995) and Neggers et al. (2004) and revised in an extensive study of marine and land shallow cumulus clouds by Sikma and Ouwersloot (2015) using systematic large-eddy experiments, we scale the cloud core vertical velocity or convective transport as a function of the convective velocity w_*:

$$w_{cc} = 0.91 w_*, \tag{E2}$$

where 0.91 is a constant estimated from a suite of numerical experiments of shallow cumulus carried out using large-eddy simulations (Sikma and Ouwersloot 2015) and w_* is the convective velocity scale of the most energetic turbulent eddies defined as

$$w_* = \left[\left(\frac{g}{\theta_o} \right) \overline{w'\theta'_v} z_i \right]^{1/3}. \tag{E3}$$

Here, g is the acceleration of gravity, θ_o is a characteristic reference potential temperature, $\overline{w'\theta'_v}$ is the buoyancy flux at the canopy top (surface), and z_i is the boundary layer height.

We subsequently parameterize the area fraction of the cloud core using the expression:

$$a_{cc} = 0.292 Q_2^{-2}, \tag{E4}$$

where 0.292 was also estimated by Sikma and Ouwersloot (2015) and Q_2 is defined as

$$Q_2 = \frac{q_t - q_s}{\sigma_q}. \tag{E5}$$

The specific humidity q_t and q_s are, respectively, the total and saturation specific humidity and σ_q (units of $\mathrm{kg_{water}^2\ kg_{atmosphere}^{-2}}$) is the spatial standard deviation of the specific humidity defined at cloud base. The σ_q parameterization at cloud base is based on the variance equation of specific humidity at cloud base (Neggers et al. 2006; van Stratum et al. 2014). The simplified parameterization reads

$$\sigma_q^2 = -\left(\overline{w'q'}\right)_e \left(\frac{\Delta q}{\Delta z}\right)\left(\frac{z_i}{w_*}\right), \tag{E6}$$

where $\left(\overline{w'q'}\right)_e$ is the entrainment flux of specific humidity at the cloud base, Δq is the discontinuity (jump) between the free troposphere and the mixed-layer values assuming an infinitesimal discontinuity, i.e., the zero-order model (Tennekes and Driedonks 1981), and Δz is the transitional layer calculated as the difference between the lifting condensation level and the boundary layer height (Augstein et al. 1974; Albrecht et al. 1979). If we parameterize $\left(\overline{w'q'}\right)_e$ using a zero-order model,

$$\left(\overline{w'q'}\right)_e = -w_e \Delta q = -\left(\frac{dz_i}{dt}\right)\Delta q. \tag{E7}$$

Here, we define the entrainment velocity w_e equal to the boundary later growth dh/dt, where we assume that there are no subsidence motions. We finally obtain the final expression for σ_q that reads

$$\sigma_q^2 = \left(\frac{dz_i}{dt}\right)\left(\frac{\Delta q^2}{\Delta z}\right)\left(\frac{z_i}{w_*}\right). \tag{E8}$$

Figure E1 shows all the variables used in the calculation of the area fraction cloud cover and mass flux for the shallow cumulus and shallow-to-deep aggregate cases. The calculations are based on two different inputs: observations and model calculations using the rain forest–atmosphere model CLASS. In general, and in spite of the oversimplification of the processes, the agreement is very satisfactory. The traveling time of the parcel (Fig. E1a) from the canopy top to the ABL height shows representative values ranging from 8 to 20 min. There is also a very good agreement between the observation calculations and the model in the calculation of the entrainment velocity (Fig. E1b), except for the time 1500 LT in which normally deep convection is the dominated process. The transitional layer (Fig. E1c) that represent the layer between moist driven turbulence [quantified by the lifting condensation level (LCL)] and dry driven turbulence (quantified by the ABL height) shows that probability of forming clouds increases during the course of the day (1200 LT values are closer to zero than 0900 LT), and also, the deep convective case show (1500 LT blue) is the only one with negative values in the calculation of the observations. Due to the overall simplifications in inferring Δ_q^2 (Fig. E1d) and $q_t - q_s$ (Fig. E1e), there is more scatter in the comparison between the model and observations, and much larger variability on the model calculations of $q_t - q_s$. However, there is an offset compensation since the final calculation of σ_q^2 at the cloud base shows a satisfactory alignment between observations and model calculations.
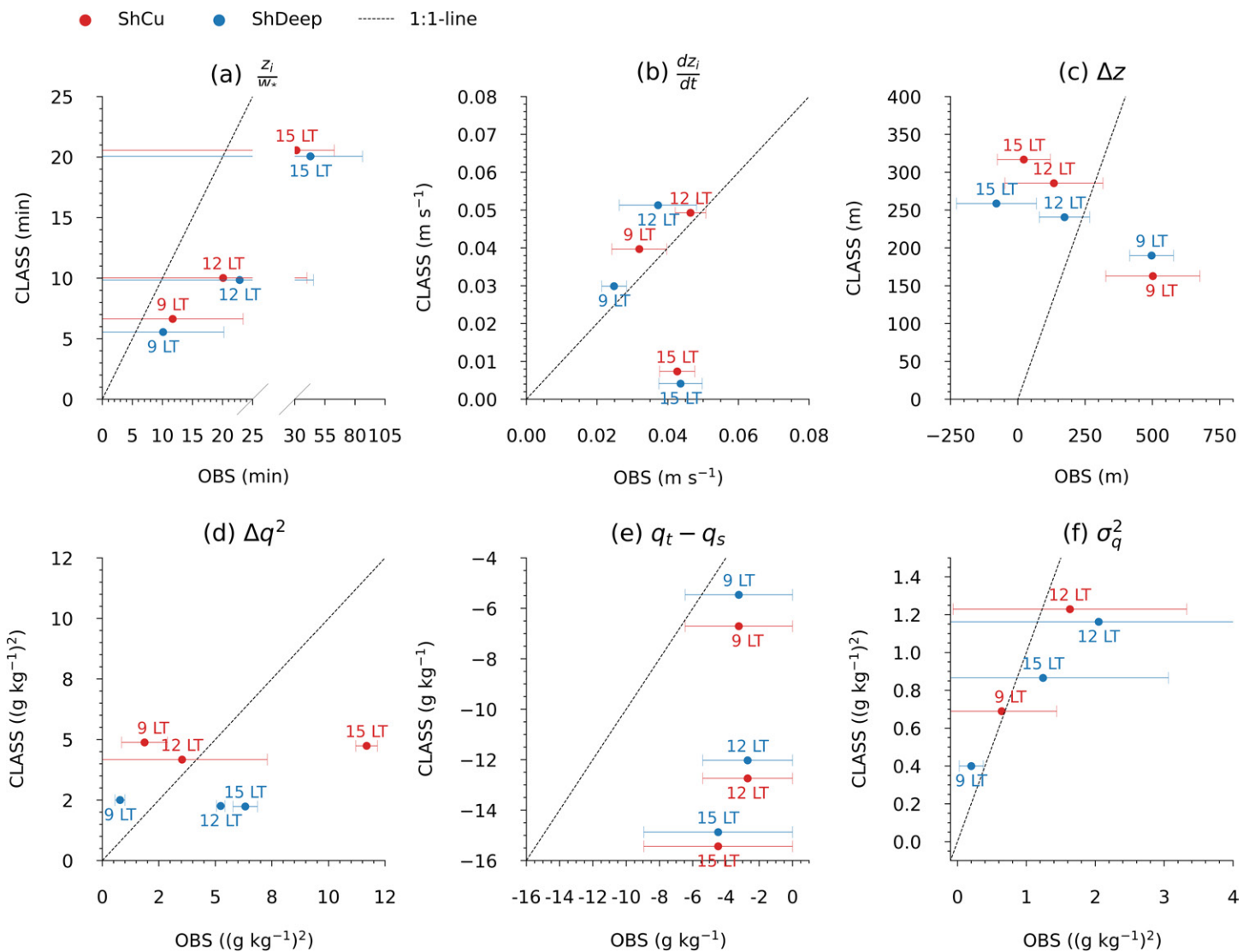
FIG. E1. Sequence of all the variables used to calculate the area fraction of the cloud core and the mass flux in Fig. 8 [Eqs. (E1)–(E8)] at the cloud base. Results are presented for the aggregate of the ShCU and ShDeep convection. The variables are calculated using the OBS (*x* axis) or the rain forest–atmosphere coupled model (*y* axis). The variables are (a) time of a parcel to move upward from the canopy top to the ABL height calculated from the ABL height and the convective velocity, (b) entrainment velocity, (c) transition layer defined as lifting condensation level minus the ABL height, (d) infinitesimal discontinuity (jump) at the ABL, (e) difference between total and saturation specific humidity, and (f) variance of the specific humidity.

References

Adnew, G. A., T. L. Pons, G. Koren, W. Peters, and T. Röckmann, 2020: Leaf-scale quantification of the effect of photosynthetic gas exchange on $\delta^{17}O$ atmospheric CO_2. *Biogeosciences*, **17**, 3903–3922, https://doi.org/10.5194/bg-17-3903-2020.

——, G. Koren, E. Melman, W. Peters, M. van, D. E. Molen, and T. Röckmann, 2022: Diurnal variation in the $\Delta'17O$ of atmospheric CO_2 in the temperate scots pine forest ecosystem. *Goldschmidt2022*, Honolulu, HI, Geochemical Society and of the European Association of Geochemistry, Abstract 12047, https://doi.org/10.46427/gold2022.12047.

Aguirre-Correa, F., J. Vilà-Guerau de Arellano, R. Ronda, F. Lobos-Roco, F. Suárez, and O. Hartogensis, 2023: Midday boundary-layer collapse in the Altiplano desert: The combined effect of advection and subsidence. *Bound.-Layer Meteor.*, **187**, 643–671, https://doi.org/10.1007/s10546-023-00790-5.

Albrecht, B. A., A. K. Betts, W. H. Schubert, and S. K. Cox, 1979: Model of the thermodynamic structure of the trade-wind boundary layer: Part I. Theoretical formulation and sensitivity tests. *J. Atmos. Sci.*, **36**, 73–89, https://doi.org/10.1175/1520-0469(1979)036<0073:MOTTSO>2.0.CO;2.

Anber, U., P. Gentine, S. Wang, and A. H. Sobel, 2015: Fog and rain in the Amazon. *Proc. Natl. Acad. Sci. USA*, **112**, 11473–11477, https://doi.org/10.1073/pnas.1505077112.

Andreae, M. O., and Coauthors, 2015: The Amazon Tall Tower Observatory (ATTO): Overview of pilot measurements on ecosystem ecology, meteorology, trace gases, and aerosols. *Atmos. Chem. Phys.*, **15**, 10723–10776, https://doi.org/10.5194/acp-15-10723-2015.

Augstein, E., H. Schmidt, and F. Ostapoff, 1974: The vertical structure of the atmospheric planetary boundary layer in undisturbed trade winds over the Atlantic Ocean. *Bound.-Layer Meteor.*, **6**, 129–150, https://doi.org/10.1007/BF00232480.

Avissar, R., P. L. Silva Dias, M. A. F. Silva Dias, and C. Nobre, 2002: The Large-Scale Biosphere-Atmosphere Experiment in Amazonia (LBA): Insights and future research needs. *J. Geophys. Res. Atmos.*, **107**, 8086, https://doi.org/10.1029/2002JD002704.

Baldocchi, D. D., and J. S. Amthor, 2001: Canopy photosynthesis: History, measurements, and models. *Terrestrial Global Productivity.* J. Roy, B. Saugier and H. A. Mooney, Eds., Academy Press, 9–31.

Barkhordarian, A., S. S. Saatchi, A. Behrangi, P. C. Loikith, and C. R. Mechoso, 2019: A recent systematic increase in vapor pressure deficit over tropical South America. *Sci. Rep.*, **9**, 15331, https://doi.org/10.1038/s41598-019-51857-8.

Betts, A. K., 1973: Non-precipitating cumulus convection and its parameterization. *Quart. J. Roy. Meteor. Soc.*, **99**, 178–196, https://doi.org/10.1002/qj.49709941915.

Biudes, M. S., G. L. Vourlitis, N. G. Machado, P. H. Z. de Arruda, G. A. R. Neves, F. de Almeida Lobo, C. M. U. Neale, and J. de Souza Nogueira, 2015: Patterns of energy exchange for tropical ecosystems across a climate gradient in Mato Grosso, Brazil. *Agric. For. Meteor.*, **202**, 112–124, https://doi.org/10.1016/j.agrformet.2014.12.008.

Bonan, G. B., E. G. Patton, J. F. Finnigan, D. D. Baldocchi, and I. H. Harman, 2021: Moving beyond the incorrect but useful paradigm: Reevaluating big-leaf and multilayer plant canopies to model biosphere-atmosphere fluxes—A review. *Agric. For. Meteor.*, **306**, 108435, https://doi.org/10.1016/j.agrformet.2021.108435.

Botía, S., and Coauthors, 2022: The CO_2 record at the Amazon Tall Tower Observatory: A new opportunity to study processes on seasonal and inter-annual scales. *Global Change Biol.*, **28**, 588–611, https://doi.org/10.1111/gcb.15905.

Boussetta, S., and Coauthors, 2013: Natural land carbon dioxide exchanges in the ECMWF integrated forecasting system: Implementation and offline validation. *J. Geophys. Res. Atmos.*, **118**, 5923–5946, https://doi.org/10.1002/jgrd.50488.

Bowling, D., P. Tans, and R. Monson, 2001: Partitioning net ecosystem carbon exchange with isotopic fluxes of CO_2. *Global Change Biol.*, **7**, 127–145, https://doi.org/10.1046/j.1365-2486.2001.00400.x.

Brienen, R. J. W., and Coauthors, 2015: Long-term decline of the Amazon carbon sink. *Nature*, **519**, 344–348, https://doi.org/10.1038/nature14283.

Cecchini, M. A., M. de Bruine, J. Vilà-Guerau de Arellano, and P. Artaxo, 2022: Quantifying vertical wind shear effects in shallow cumulus clouds over Amazonia. *Atmos. Chem. Phys.*, **22**, 11867–11888, https://doi.org/10.5194/acp-22-11867-2022.

Costa, M. H., and J. A. Foley, 2000: Combined effects of deforestation and doubled atmospheric CO_2 concentrations on the climate of Amazonia. *J. Climate*, **13**, 18–34, https://doi.org/10.1175/1520-0442(2000)013<0018:CEODAD>2.0.CO;2.

Cuijpers, J. W. M., and P. Bechtold, 1995: A simple parameterization of cloud water related variables for use in boundary layer models. *J. Atmos. Sci.*, **52**, 2486–2490, https://doi.org/10.1175/1520-0469(1995)052<2486:ASPOCW>2.0.CO;2.

Czikowsky, M. J., and D. R. Fitzjarrald, 2009: Detecting rainfall interception in an Amazonian rain forest with eddy flux measurements. *J. Hydrol.*, **377**, 92–105, https://doi.org/10.1016/j.jhydrol.2009.08.002.

de Feiter, V. S., 2023: CloudRoots: Moist air intrusion and vertical wind shear as limiting factors for deep convective development. M.S. thesis, Dept. of Meteorology and Air Quality Section, Wageningen University, 34 pp.

Dias-Júnior, C. Q., and Coauthors, 2019: Is there a classical inertial sublayer over the Amazon forest? *Geophys. Res. Lett.*, **46**, 5614–5622, https://doi.org/10.1029/2019GL083237.

——, and Coauthors, 2022: Intercomparison of planetary boundary layer heights using remote sensing retrievals and ERA5 reanalysis over central Amazonia. *Remote Sens.*, **14**, 4561, https://doi.org/10.3390/rs14184561.

Doutriaux-Boucher, M., M. J. Webb, J. M. Gregory, and O. Boucher, 2009: Carbon dioxide induced stomatal closure increases radiative forcing via a rapid reduction in low cloud. *Geophys. Res. Lett.*, **36**, L02703, https://doi.org/10.1029/2008GL036273.

Drueke, S., D. J. Kirshbaum, and P. Kollias, 2021: Environmental sensitivities of shallow-cumulus dilution—Part 2: Vertical wind profile. *Atmos. Chem. Phys.*, **21**, 14039–14058, https://doi.org/10.5194/acp-21-14039-2021.

Durand, M., E. H. Murchie, A. V. Lindfors, O. Urban, P. J. Aphalo, and T. M. Robson, 2021: Diffuse solar radiation and canopy photosynthesis in a changing environment. *Agric. For. Meteor.*, **311**, 108684, https://doi.org/10.1016/j.agrformet.2021.108684.

Findell, K. L., P. Gentine, B. R. Lintner, and C. Kerr, 2011: Probability of afternoon precipitation in eastern United States and Mexico enhanced by high evaporation. *Nat. Geosci.*, **4**, 434–439, https://doi.org/10.1038/ngeo1174.

Fitzjarrald, D. R., B. L. Stormwind, G. Fisch, and O. M. R. Cabral, 1988: Turbulent transport observed just above the Amazon forest. *J. Geophys. Res.*, **93**, 1551–1563, https://doi.org/10.1029/JD093iD02p01551.

Friedlingstein, P., and Coauthors, 2022: Global carbon budget 2021. *Earth Syst. Sci. Data*, **14**, 1917–2005, https://doi.org/10.5194/essd-14-1917-2022.

Fu, R., L. Yin, W. Li, and R. B. Myneni, 2013: Increased dry-season length over southern Amazonia in recent decades and its implication for future climate projection. *Proc. Natl. Acad. Sci. USA*, **110**, 18110–18115, https://doi.org/10.1073/pnas.1302584110.

Garstang, M., and D. R. Fitzjarrald, 1999: *Observations of Surface to the Atmosphere Interactions in the Tropics.* Oxford University Press, 405 pp.

Gehre, M., H. Geilmann, J. Richter, R. A. Werner, and W. A. Brand, 2004: Continuous flow $^2H/^1H$ and $^{18}O/^{16}O$ analysis of water samples with dual inlet precision. *Rapid Commun. Mass Spectrom.*, **18**, 2650–2660, https://doi.org/10.1002/rcm.1672.

Gentine, P., A. A. M. Holtslag, F. D'Andrea, and M. Ek, 2013: Surface and atmospheric controls on the onset of moist convection over land. *J. Hydrometeor.*, **14**, 1443–1462, https://doi.org/10.1175/JHM-D-12-0137.1.

——, A. Massmann, B. R. Lintner, S. Hamed Alemohammad, R. Fu, J. K. Green, D. Kennedy, and J. Vilà-Guerau de Arellano, 2019: Land–atmosphere interactions

in the tropics—A review. *Hydrol. Earth Syst. Sci.*, **23**, 4171–4197, https://doi.org/10.5194/hess-23-4171-2019.

Griffis, T. J., 2013: Tracing the flow of carbon dioxide and water vapor between the biosphere and atmosphere: A review of optical isotope techniques and their application. *Agric. For. Meteor.*, **174–175**, 85–109, https://doi.org/10.1016/j.agrformet.2013.02.009.

——, and Coauthors, 2016: Investigating the source, transport, and isotope composition of water vapor in the planetary boundary layer. *Atmos. Chem. Phys.*, **16**, 5139–5157, https://doi.org/10.5194/acp-16-5139-2016.

Harman, I. N., 2012: The role of roughness sublayer dynamics within surface exchanges schemes. *Bound.-Layer Meteor.*, **142** (1), 1–20, https://doi.org/10.1007/s10546-011-9651-z.

Harriss, R. C., and Coauthors, 1990: The Amazon Boundary Layer Experiment: Wet season 1987. *J. Geophys. Res.*, **95**, 16721–16736, https://doi.org/10.1029/JD095iD10p16721.

Henkes, A., G. Fisch, L. A. T. Machado, and J.-P. Chaboureau, 2021: Morning boundary layer conditions for shallow to deep convective cloud evolution during the dry season in the central Amazon. *Atmos. Chem. Phys.*, **21**, 13207–13225, https://doi.org/10.5194/acp-21-13207-2021.

Heus, T., and Coauthors, 2010: Formulation and numerical studies by the Dutch Atmospheric Large-Eddy Simulation (DALES) and overview of its applications. *Geosci. Model Dev.*, **3**, 415–444, https://doi.org/10.5194/gmd-3-415-2010.

Heusinkveld, B. G., W. B. Mol, and C. C. van Heerwaarden, 2023: A new accurate low-cost instrument for fast synchronized spatial measurements of light spectra. *Atmos. Meas. Tech.*, **16**, 3767–3785, https://doi.org/10.5194/amt-16-3767-2023.

Horn, G. L., H. G. Ouwersloot, J. Vilà-Guerau de Arellano, and M. Sikma, 2015: Cloud shading effects on characteristic boundary-layer length scales. *Bound.-Layer Meteor.*, **157**, 237–263, https://doi.org/10.1007/s10546-015-0054-4.

Hubau, W., and Coauthors, 2020: Asynchronous carbon sink saturation in African and Amazonian tropical forests. *Nature*, **579**, 80–87, https://doi.org/10.1038/s41586-020-2035-0.

Jiménez-Rodríguez, C. D., M. Coenders-Gerrits, J. Wenninger, A. Gonzalez-Angarita, and H. Savenije, 2020: Contribution of understory evaporation in a tropical wet forest during the dry season. *Hydrol. Earth Syst. Sci.*, **24**, 2179–2206, https://doi.org/10.5194/hess-24-2179-2020.

Karl, T., A. Guenther, A. Turnipseed, P. Artaxo, and S. T. Martin, 2009: Rapid formation of isoprene photo-oxidation products observed in Amazonia. *Atmos. Chem. Phys.*, **9**, 7753–7769, https://doi.org/10.5194/acp-9-7753-2009.

Kivalov, S. N., and D. R. Fitzjarrald, 2018: Quantifying and modelling the effect of cloud shadows on the surface irradiance at tropical and midlatitude forests. *Bound.-Layer Meteor.*, **166**, 165–198, https://doi.org/10.1007/s10546-017-0301-y.

——, and ——, 2019: Observing the whole-canopy short-term dynamic response to natural step changes in incident light: Characteristics of tropical and temperate forests. *Bound.-Layer Meteor.*, **173** (1), 1–52, https://doi.org/10.1007/s10546-019-00460-5.

Knohl, A., and N. Buchmann, 2005: Partitioning the net CO_2 flux of a deciduous forest into respiration and assimilation using stable carbon isotopes. *Global Biogeochem. Cycles*, **19**, GB4008, https://doi.org/10.1029/2004GB002301.

Komiya, S., F. Kondo, T. Moossen, T. Seifert, U. Schultz, H. Geilmann, D. Walter, and J. V. Lavric, 2021: Characterizing water vapour concentration dependence of commercial cavity ring-down spectrometers for continuous on-site atmospheric water vapour isotope measurements in the tropics. *Atmos. Meas. Tech.*, **14**, 1439–1455, https://doi.org/10.5194/amt-14-1439-2021.

Lee, X., J. Huang, and E. G. Patton, 2012: A large-eddy simulation study of water vapor and carbon dioxide isotopes in the atmospheric boundary layer. *Bound.-Layer Meteor.*, **145**, 229–248, https://doi.org/10.1007/s10546-011-9631-3.

LeMone, M. A., and W. T. Pennel, 1976: The relationship of trade wind cumulus distribution to subcloud layer fluxes and structure. *Mon. Wea. Rev.*, **104**, 524–539, https://doi.org/10.1175/1520-0493(1976)104<0524:TROTWC>2.0.CO;2.

Lohou, F., and E. G. Patton, 2014: Surface energy balance and buoyancy response to shallow cumulus shading. *J. Atmos. Sci.*, **71**, 665–682, https://doi.org/10.1175/JAS-D-13-0145.1.

Longo, M., and Coauthors, 2020: Impacts of degradation on water, energy, and carbon cycling of the Amazon tropical forests. *J. Geophys. Res. Biogeosci.*, **125**, e2020JG005677, https://doi.org/10.1029/2020JG005677.

Machado, L. A. T., 2000: The Amazon energy budget using the ABLE-2B and FluAmazon data. *J. Atmos. Sci.*, **57**, 3131–3144, https://doi.org/10.1175/1520-0469(2000)057<3131:TAEBUT>2.0.CO;2.

——, and Coauthors, 2014: The CHUVA project: How does convection vary across Brazil? *Bull. Amer. Meteor. Soc.*, **95**, 1365–1380, https://doi.org/10.1175/BAMS-D-13-00084.1.

——, and Coauthors, 2021: How weather events modify aerosol particle size distributions in the Amazon boundary layer. *Atmos. Chem. Phys.*, **21**, 18065–18086, https://doi.org/10.5194/acp-21-18065-2021.

Mangan, M. R., and Coauthors, 2023: The surface-boundary layer connection across spatial scales of irrigation-driven thermal heterogeneity: An integrated data and modeling study of the LIAISE field campaign. *Agric. For. Meteor.*, **335**, 109452, https://doi.org/10.1016/j.agrformet.2023.109452.

Martin, C. L., D. Fitzjarrald, M. Garstang, A. P. Oliveira, S. Greco, and E. Brodwell, 1988: Structure and growth of the mixing layer over the Amazonian rain forest. *J. Geophys. Res.*, **93**, 1361–1375, https://doi.org/10.1029/JD093iD02p01361.

Martin, S. T., and Coauthors, 2017: The Green Ocean Amazon Experiment (GoAmazon2014/5) observes pollution affecting gases, aerosols, clouds, and rainfall over the rain forest. *Bull. Amer. Meteor. Soc.*, **98**, 981–997, https://doi.org/10.1175/BAMS-D-15-00221.1.

Misson, L., and Coauthors, 2007: Partitioning forest carbon fluxes with overstory and understory eddy-covariance measurements: A synthesis based on FLUXNET data. *Agric. For. Meteor.*, **144**, 14–31, https://doi.org/10.1016/j.agrformet.2007.01.006.

Moene, A. F., and J. C. van Dam, 2014: *Transport in the Atmosphere-Vegetation-Soil Continuum.* Cambridge University Press, 436 pp.

Mol, W. B., B. J. H. van Stratum, W. H. Knap, and C. C. van Heerwaarden, 2023: Reconciling observations of solar irradiance variability with cloud size distributions. *J. Geophys. Res. Atmos.*, **128**, e2022JD037894, https://doi.org/10.1029/2022JD037894.

Moonen, R. P. J., G. A. Adnew, O. K. Hartogensis, J. Vilà-Guerau de Arellano, D. J. Bonell Fontas, and T. Röckmann, 2023: Data treatment and corrections for estimating H_2O and CO_2 isotope fluxes from high-frequency observations. *Atmos. Meas. Tech.*, **16**, 5787–5810, https://doi.org/10.5194/amt-16-5787-2023.

Neggers, R. A. J., A. P. Siebesma, G. Lenderink, and A. A. M. Holtslag, 2004: An evaluation of mass flux closures for diurnal cycles of shallow cumulus. *Mon. Wea. Rev.*, **132**, 2525–2538, https://doi.org/10.1175/MWR2776.1.

——, B. Stevens, and J. D. Neelin, 2006: A simple equilibrium model for shallow-cumulus-topped mixed layers. *Theor. Comput. Fluid Dyn.*, **20**, 305–322, https://doi.org/10.1007/s00162-006-0030-1.

Nölscher, A. C., A. M. Yañez-Serrano, S. Wolff, J. V. de Araujo, J. V. Lavrič, J. Kesselmeier, and J. Williams, 2016: Unexpected seasonality in quantity and composition of Amazon rainforest air reactivity. *Nat. Commun.*, **7**, 10383, https://doi.org/10.1038/ncomms10383.

Ouwersloot, H. G., J. Vilá-Guerau de Arellano, B. J. H. van Stratum, M. C. Krol, and J. Lelieveld, 2013: Quantifying the transport of subcloud layer reactants by shallow cumulus clouds over the Amazon. *J. Geophys. Res. Atmos.*, **118**, 13041–13059, https://doi.org/10.1002/2013JD020431.

——, A. F. Moene, J. J. Attema, and J. Vilà-Guerau de Arellano, 2017: Large-eddy simulation comparison of neutral flow over a canopy: Sensitivity to physical and numerical conditions, and similarity to other representations. *Bound.-Layer Meteor.*, **162**, 71–89, https://doi.org/10.1007/s10546-016-0182-5.

Park, S., J. Kug, S. Jun, S. Jeong, and J. Kim, 2021: Role of cloud feedback in continental warming response to CO_2 physiological forcing. *J. Climate*, **34**, 8813–8828, https://doi.org/10.1175/JCLI-D-21-0025.1.

Parker, G. G., D. R. Fitzjarrald, and I. C. Gonçalves Sampaio, 2019: Consequences of environmental heterogeneity for the photosynthetic light environment of

a tropical forest. *Agric. For. Meteor.*, **278**, 107661, https://doi.org/10.1016/j.agrformet.2019.107661.

Pataki, D. E., and Coauthors, 2003: The application and interpretation of keeling plots in terrestrial carbon cycle research. *Global Biogeochem. Cycles*, **17**, 1022, https://doi.org/10.1029/2001GB001850.

Patton, E. G., P. P. Sullivan, R. H. Shaw, J. J. Finnigan, and J. C. Weil, 2016: Atmospheric stability influences on coupled boundary layer and canopy turbulence. *J. Atmos. Sci.*, **73**, 1621–1647, https://doi.org/10.1175/JAS-D-15-0068.1.

Pedruzo-Bagazgoitia, X., H. G. Ouwersloot, M. Sikma, C. C. van Heerwaarden, C. M. J. Jacobs, and J. Vilà-Guerau de Arellano, 2017: Direct and diffuse radiation in the shallow cumulus-vegetation system: Enhanced and decreased evapotranspiration regimes. *J. Hydrometeor.*, **18**, 1731–1748, https://doi.org/10.1175/JHM-D-16-0279.1.

——, and Coauthors, 2023: Investigating the diurnal radiative, turbulent and biophysical processes in the Amazonian canopy-atmosphere interface by combining les simulations and observations. *J. Adv. Model. Earth Syst.*, **15**, e2022MS003210, https://doi.org/10.1029/2022MS003210.

Pfannerstill, E. Y., and Coauthors, 2021: Total OH reactivity over the Amazon rainforest: Variability with temperature, wind, rain, altitude, time of day, season and an overall budget closure. *Atmos. Chem. Phys.*, **21**, 6231–6256, https://doi.org/10.5194/acp-21-6231-2021.

Pietschnig, M., A. L. S. Swann, F. H. Lambert, and G. K. Vallis, 2021: Response of tropical rainfall to reduced evapotranspiration depends on continental extent. *J. Climate*, **34**, 9221–9234, https://doi.org/10.1175/JCLI-D-21-0195.1.

Roberts, J., O. M. R. Cabral, and L. F. D. Aguiar, 1990: Stomatal and boundary-layer conductances in an Amazonian terra firme rain forest. *J. Appl. Ecol.*, **27**, 336–353, https://doi.org/10.2307/2403590.

Rösner, B., I. Benedict, C. Van Heerwaarden, A. Weerts, W. Hazeleger, P. Bissolli, and K. Trachte, 2018: The long heat wave and drought in Europe in 2018 [in "State of the Climate in 2018"]. *Bull. Amer. Meteor. Soc.*, **100** (9), S222–S223.

Rothfuss, Y., I. Braud, N. Le Moine, P. Biron, J.-L. Durand, M. Vauclin, and T. Bariac, 2012: Factors controlling the isotopic partitioning between soil evaporation and plant transpiration: Assessment using a multi-objective calibration of SiSPAT-isotope under controlled conditions. *J. Hydrol.*, **442–443**, 75–88, https://doi.org/10.1016/j.jhydrol.2012.03.041.

Shaw, R. H., J. Tavangar, and D. P. Ward, 1983: Structure of the Reynolds stress in a canopy layer. *J. Climate Appl. Meteor.*, **22**, 1922–1931, https://doi.org/10.1175/1520-0450(1983)022<1922:SOTRSI>2.0.CO;2.

Sikma, M., and H. G. Ouwersloot, 2015: Parameterizations for convective transport in various cloud-topped boundary layers. *Atmos. Chem. Phys.*, **15**, 10399–10410, https://doi.org/10.5194/acp-15-10399-2015.

——, and J. Vilà-Guerau de Arellano, 2019: Substantial reductions in cloud cover and moisture transport by dynamic plant responses. *Geophys. Res. Lett.*, **46**, 1870–1878, https://doi.org/10.1029/2018GL081236.

——, ——, X. Pedruzo-Bagazgoitia, T. Voskamp, B. Heusinkveld, N. Anten, and J. B. Evers, 2019: Impact of future warming and enhanced [CO_2] on the vegetation-cloud interaction. *J. Geophys. Res. Atmos.*, **124**, 12444–12454, https://doi.org/10.1029/2019JD030717.

Spracklen, D. V., S. R. Arnold, and C. M. Taylor, 2012: Observations of increases tropical rainfall preceded by air passage over forests. *Nature*, **489**, 282–285, https://doi.org/10.1038/nature11390.

Staal, A., O. A. Tuinenburg, J. H. C. Bosmans, M. Holmgren, E. H. van Nes, M. Scheffer, D. C. Zemp, and S. C. Dekker, 2018: Forest-rainfall cascades buffer against drought across the Amazon. *Nat. Climate Change*, **8**, 539–543, https://doi.org/10.1038/s41558-018-0177-y.

Sullivan, P. P., C. Moeng, B. Stevens, D. H. Lenschow, and S. D. Mayor, 1998: Structure of the entrainment zone capping the convective atmospheric boundary layer. *J. Atmos. Sci.*, **55**, 3042–3064, https://doi.org/10.1175/1520-0469(1998)055<3042:SOTEZC>2.0.CO;2.

Taylor, C. M., A. Gounou, F. Guicahrd, P. H. Harris, R. J. Ellis, F. Couvreux, and M. De Kauwe, 2011: Frequency of Sahelian storm initiation enhanced over

mesoscale soil-moisture patterns. *Nat. Geosci.*, **4**, 430–433, https://doi.org/10.1038/ngeo1173.

Tennekes, H., and A. G. M. Driedonks, 1981: Basic entrainment equations for the atmospheric boundary layer. *Bound.-Layer Meteor.*, **20**, 515–531, https://doi.org/10.1007/BF00122299.

Thomas, C., J. Martin, M. Goeckede, M. Siqueira, T. Foken, B. Law, H. Loescher, and G. Katul, 2008: Estimating daytime subcanopy respiration from conditional sampling methods applied to multi-scalar high frequency turbulence time series. *Agric. For. Meteor.*, **148**, 1210–1229, https://doi.org/10.1016/j.agrformet.2008.03.002.

Trenberth, K. E., 1999: Atmospheric moisture recycling: Role of advection and local evaporation. *J. Climate*, **12**, 1368–1381, https://doi.org/10.1175/1520-0442(1999)012<1368:AMRROA>2.0.CO;2.

van Asperen, H., S. Komiya, S. Jones, J. Botia, J. Lavric, T. Warneke, D. Griffith, and S. Trumbore, 2023: Unique tall tower greenhouse gas measurements in the Amazon rainforest: Observed patterns and daily cycles. *EGU General Assembly*, Vienna, Austria, European Geophysical Union, EGU23-10522, https://doi.org/10.5194/egusphere-egu23-10522, 2023.

van Heerwaarden, C. C., and A. J. Teuling, 2014: Disentangling the response of forest and grassland energy exchange to heatwaves under idealized land–atmosphere coupling. *Biogeosciences*, **11**, 6159–6171, https://doi.org/10.5194/bg-11-6159-2014.

van Kesteren, B., O. K. Hartogensis, D. van Dinther, A. F. Moene, H. A. R. De Bruin, and A. A. M. Holtslag, 2013: Measuring H_2O and CO_2 fluxes at field scales with scintillometry: Part II—Validation and application of 1-min flux estimates. *Agric. For. Meteor.*, **178–179**, 88–105, https://doi.org/10.1016/j.agrformet.2013.01.010.

van Stratum, B. J. H., J. Vilá-Guerau de Arellano, C. C. van Heerwaarden, and H. G. Ouwersloot, 2014: Subcloud-layer feedbacks driven by the mass flux of shallow cumulus convection over land. *J. Atmos. Sci.*, **71**, 881–895, https://doi.org/10.1175/JAS-D-13-0192.1.

Veerman, M. A., X. Pedruzo-Bagazgoitia, F. Jakub, J. Vilà-Guerau de Arellano, and C. C. van Heerwaarden, 2020: Three-dimensional radiative effects by shallow cumulus clouds on dynamic heterogeneities over a vegetated surface. *J. Adv. Model. Earth Syst.*, **12**, e2019MS001990, https://doi.org/10.1029/2019MS001990.

Vilà-Guerau de Arellano, J., B. Gioli, F. Miglietta, H. Jonker, H. Baltink, R. Hutjes, and A. Holtslag, 2004: Entrainment process of carbon dioxide in the atmospheric boundary layer. *J. Geophys. Res.*, **109**, D18110, https://doi.org/10.1029/2004JD004725.

——, C. H. van Heerwaarden, and J. Lelieveld, 2012: Modelled suppression of boundary-layer clouds by plants in a CO_2-rich atmosphere. *Nat. Geosci.*, **5**, 701–704, https://doi.org/10.1038/ngeo1554.

——, C. C. van Heerwaarden, B. J. H. van Stratum, and K. van den Dries, 2015: *Atmospheric Boundary Layer: Integrating Air Chemistry and Land Interactions.* Cambridge University Press, 265 pp.

——, G. Koren, H. G. Ouwersloot, I. van der Velde, T. Röckmann, and J. B. Miller, 2019: Sub-diurnal variability of the carbon dioxide and water vapor isotopologues at the field observational scale. *Agric. For. Meteor.*, **275**, 114–135, https://doi.org/10.1016/j.agrformet.2019.05.014.

——, and Coauthors, 2020: CloudRoots: Integration of advanced instrumental techniques and process modelling of sub-hourly and sub-kilometre land–atmosphere interactions. *Biogeosciences*, **17**, 4375–4404, https://doi.org/10.5194/bg-17-4375-2020.

——, and Coauthors, 2023: Advancing understanding of land–atmosphere interactions by breaking discipline and scale barriers. *Ann. N. Y. Acad. Sci.*, **1522**, 74–97, https://doi.org/10.1111/nyas.14956.

Wehr, R., J. W. Munger, D. D. Nelson, J. B. McManus, M. S. Zahniser, S. C. Wofsy, and S. R. Saleska, 2013: Long-term eddy covariance measurements of the isotopic composition of the ecosystem-atmosphere exchange of CO_2 in a temperate forest. *Agric. For. Meteor.*, **181**, 69–84, https://doi.org/10.1016/j.agrformet.2013.07.002.

Welp, L. R., and Coauthors, 2012: A meta-analysis of water vapor deuterium-excess in the midlatitude atmospheric surface layer. *Global Biogeochem. Cycles*, **26**, GB3021, https://doi.org/10.1029/2011GB004246.

Werner, R. A., M. Rothe, and W. A. Brand, 2001: Extraction of CO_2 from air samples for isotopic analysis and limits to ultra high precision $\delta^{18}O$ determination in CO_2 gas. *Rapid Commun. Mass Spectrom.*, **15**, 2152–2167, https://doi.org/10.1002/rcm.487.

Winderlich, J., and Coauthors, 2010: Continuous low-maintenance $CO_2/CH_4/H_2O$ measurements at the Zotino Tall Tower Observatory (ZOTTO) in central Siberia. *Atmos. Meas. Tech.*, **3**, 1113–1128, https://doi.org/10.5194/amt-3-1113-2010.

Xiao, W., Z. Wei, and X. Wen, 2018: Evapotranspiration partitioning at the ecosystem scale using the stable isotope method—A review. *Agric. For. Meteor.*, **263**, 346–361, https://doi.org/10.1016/j.agrformet.2018.09.005.

Yakir, D., J. A. Berry, L. Giles, and C. B. Osmond, 1994: Isotopic heterogeneity of water in transpiring leaves: Identification of the component that controls the $\delta^{18}O$ of atmospheric O_2 and CO_2. *Plant Cell Environ.*, **17**, 73–80, https://doi.org/10.1111/j.1365-3040.1994.tb00267.x.

Zemp, D. C., C.-F. Schleussner, H. M. J. Barbosa, R. J. van der Ent, J. F. Donges, J. Heinke, G. Sampaio, and A. Rammig, 2014: On the importance of cascading moisture recycling in South America. *Atmos. Chem. Phys.*, **14**, 13 337–13 359, https://doi.org/10.5194/acp-14-13337-2014.

Zhang, J., T. J. Griffis, and J. M. Baker, 2006: Using continuous stable isotope measurements to partition net ecosystem CO_2 exchange. *Plant Cell Environ.*, **29**, 483–496, https://doi.org/10.1111/j.1365-3040.2005.01425.x.